Structure and mechanism of a phage-encoded SAM lyase revises catalytic function of enzyme family

Xiaohu Guo[1,5#], Annika Söderholm[1#], Sandesh Kanchugal P[1#], Geir Villy Isaksen[1,2#], Omar Warsi[3], Ulrich Eckhard[1,6], Silvia Trigüis[1], Adolf Gogoll[4], Jon Jerlström-Hultqvist[3,1], Johan Åqvist[1], Dan I. Andersson[3] & Maria Selmer[1*]

[1] Department of Cell and Molecular Biology, Uppsala University, BMC, Box 596, 751 24 Uppsala, Sweden

[2] Hylleraas Centre for Quantum Molecular Sciences, Department of Chemistry, UiT - The Arctic University of Norway, N9037, Tromsø, Norway.

[3] Department of Medical Biochemistry and Microbiology, Uppsala University, BMC, Box 582, 751 23 Uppsala, Sweden

[4] Department of Chemistry-BMC, Uppsala University, BMC, Box 576, 75123, Uppsala, Sweden

[5] Current affiliation: Division of Biochemistry, Cancer Genomics Center, Netherlands Cancer Institute, Amsterdam, the Netherlands

[6] Current affiliation: Proteolysis Lab, Department of Structural Biology, Molecular Biology Institute of Barcelona, CSIC, Barcelona Science Park, Baldiri Reixac, 15-21, 08028 Barcelona, Catalonia, Spain.

[#] These authors contributed equally to this study.

* to whom correspondence should be addressed: maria.selmer@icm.uu.se

Abstract

The first SAM degrading enzyme (SAMase) was discovered in bacteriophage T3, as a counter-defense against the bacterial restriction-modification system, and annotated as an S-adenosyl-L-methionine (SAM) hydrolase forming 5'-methyl-thioadenosine (MTA) and L-homoserine. From environmental phages, we recently discovered three SAMases with barely detectable sequence similarity to T3 SAMase and without homology to proteins of known structure. Here, we present the very first phage SAMase structures, in complex with a substrate analogue and the product MTA. The structure shows a trimer of alpha-beta sandwiches similar to the GlnB-like superfamily, with active sites formed at the trimer interfaces. Quantum-mechanical calculations, thin-layer chromatography and NMR spectroscopy demonstrate that this family of enzymes are not hydrolases but lyases forming MTA and L-homoserine lactone in a unimolecular reaction mechanism. Sequence analysis, *in vitro* and *in vivo* mutagenesis support that T3 SAMase belongs to the same structural family and utilizes the same reaction mechanism.

Introduction

S-adenosyl methionine (SAM) plays many important roles in biology. It is an essential methyl donor for methyltransferases that act on nucleic acids, proteins, lipids and small molecules, but is also involved in many other reactions, *e.g.* as a substrate used in biosynthesis of polyamines and quorum sensing molecules (reviewed in (Loenen, 2006)). It is also involved in epigenetic changes in many organisms (Janke et al., 2015; Su et al., 2016) and in bacterial restriction-modification systems where methylation of DNA is used to distinguish foreign DNA from host DNA (Wilson and Murray, 1991).

In early studies of nucleic acid methylation, it was observed that while infection of *E. coli* with phage T1, T2 and T4 induced higher levels of DNA methylation, infection with phage T3 reduced the degree of methylation of not only DNA, but also tRNA and rRNA (Gold and Hurwitz, 1964). The reduction of methylation by T3 infection was associated with an immediate and dramatic lowering of the level of S-adenosyl methionine (SAM) in the *E. coli* cell extract. The degradation products were, using paper chromatography and chemical tests, identified as 5'-methyl-thioadenosine (MTA) and L-homoserine (Gold and Hurwitz, 1964) (Fig. 1, top), which led to the claimed discovery of a potent T3-encoded SAM hydrolase enzyme (Hausmann, 1967).

Subsequent work showed that the T3 SAMase was produced early in infection (Gefter et al., 1966), encoded in the early transcribed portion of the phage genome (Herrlich and Schweiger, 1970) and important for the counter defense of the bacteriophage against the type I restriction modification (RM) system of the host bacterium. In this type of RM system, SAM is an essential cofactor for both methylation of host DNA and restriction of target sequences in the foreign DNA. Two potential mechanisms for how the RM system could be impaired were presented. First, the lowered SAM levels prevented methylation of the host genome and the SAM-dependent restriction of the phage genome (Krueger et al., 1975).

Second, inhibition was observed to be independent of SAM degradation and possibly linked to an interaction with the restriction enzyme (Spoerel et al., 1979; Studier and Movva, 1976).

Recently, three additional SAM degrading enzymes were identified in a screen for bacteriophage DNA that could rescue an auxotrophic *E. coli* mutant where the isoleucine biosynthetic *ilvA* gene was deleted. Investigations using proteomics and RNA-seq showed that the phage-encoded polypeptides induced up-regulation of the biosynthetic pathway for methionine by degradation of SAM (Jerlström Hultqvist et al., 2018), which together with the repressor protein MetJ acts as a co-repressor of the *met* regulon (Weissbach and Brot, 1991). Isoleucine biosynthesis was rescued through a promiscuous activity of one of the up-regulated enzymes, MetB (Fig. S1). One of the newly identified SAM degrading enzymes, Svi3-3, was cloned, expressed and purified. *In vitro* activity assays demonstrated that Svi3-3 catalyzed conversion of SAM to MTA.

We herein present the first structure of a phage-encoded SAMase and explore the reaction mechanism using both computational and experimental biochemistry. Strikingly, the results unambiguously show that the phage-encoded SAMases are not hydrolases, as believed since the 1960s, but lyases (Fig. 1).

Results

Structure determination of a SAM hydrolase enzyme

The Svi3-3 enzyme was originally expressed from a library of fragmented environmental phage DNA. For this reason, the exact size of the original open reading frame was unknown, but an N-terminally hexahistidine-tagged 162 amino acid construct including some vector-derived sequence was shown to have SAMase activity (Jerlström Hultqvist et al., 2018). The phage-derived sequence was subcloned to allow proteolytic removal of the hexahistidine tag, and based on predictions of a disordered N terminus, truncated variants were made. Full-

length and N-terminally truncated variants of Svi3-3 were expressed with an N-terminal hexahistidine tag and purified on a Ni-column for structural studies. When expressed from the T7-promoter expression plasmid, the proteins were highly toxic and the tightly regulated, arabinose-inducible BL21 (AI) cells had to be used to allow cell growth until induction. An N-terminally truncated 146 amino acid construct of Svi3-3, where the hexahistidine tag had been removed (Table S1), formed crystals in presence of SAM or the analogue S-adenosyl homocysteine (SAH). We here number its sequence starting at the N terminus of the TEV-cleaved protein, corresponding to an offset of -16 in relation to previous work (Jerlström Hultqvist et al., 2018). The crystals diffracted to 1.45 Å resolution in space group $F4_132$ and the structure was solved using *ab initio* methods with Arcimboldo (Rodríguez et al., 2009) (Fig. 2A, F). There is one monomer in the asymmetric unit, forming a trimer around the 3-fold crystallographic axis. Apart from the disordered C-terminal 16 residues, the full structure could be built.

Structure of Svi3-3

Svi3-3 forms a trimer of ferredoxin-like fold alpha-beta sandwiches, where each subunit has two helices on the outside and a five-stranded anti-parallel beta sheet at the center (Fig. 2A-B). The subunits pack in a triangular manner, forming continuous beta sheets with their neighbors and are each in a "velcro-like" topology where residue 2-6 at the N-terminus of one subunit form beta-sheet interactions with residue 120-124 in β8 of another subunit (Fig. 2A). The long β5 forms beta-sheet interactions with both of the other monomers through interactions between the backbones around residue 51 and 55. In addition, the end of the β5-β6 hairpin packs against α1 of another monomer. The trimer interfaces are each stabilized by a single salt bridge, numerous hydrogen bonds and by hydrophobic interactions at the center.

The substrate analogue SAH binds at the interface between two subunits (Fig. 2C-D), enclosed by the β5-β6 hairpin at the edge of the sheet. The adenosine base is recognized by interactions with the backbone carbonyl and amide of Ile77 and the side chain of Ser50. The ribose forms interactions with Ser50 from one subunit and Glu69 and Ser71 from the other subunit. The homoserine moiety forms interactions with backbone groups and the side chains of Glu69 and Gln104. In the structure from co-crystallization with SAM, catalysis has occurred and the product MTA is observed in identical position as the corresponding part of SAH, with the methyl group pointing away from Glu69 (Fig. 2E-F), while a proline molecule from the cryo buffer is bound in the second half of the active site, mimicking the second product. The protein structures are virtually identical in presence of SAH and MTA (root mean square deviation (RMSD) of 0.16 Å over 129 C_α atoms). To test if the structure contains all the elements needed for activity *in vivo*, and because the start and end of the native phage protein sequence remains unknown, constructs truncated to only contain the ordered parts were tested for their ability to rescue the *ilvA* knockout mutant. Indeed, the N-terminally truncated construct additionally lacking the disordered C-terminus provided similar rescue to full-length Svi3-3, indicating that neither tail is needed for SAMase activity (data not shown). Based on this result, all further experiments were performed with the 146 amino acid Svi3-3 construct (Table S1).

Crystallization in absence of ligands led to a lower-resolution apo structure. The structure of Svi3-3 in apo state is overall very similar to the complex structures (RMSD of 0.84 Å over 124 C_α atoms), but there is a shift of the N-terminus, a conformational change of residues 7-9 to form a more extensive interaction with β9 and the preceding loop of the neighboring subunit, leading to a slight loosening of the trimer (Fig. 3). In addition, residues 64-65 in the β7- β8 hairpin are disordered.

Small angle X-ray scattering (SAXS) data confirmed that Svi3-3 has a similar trimeric structure in apo state as in presence of SAM (Fig. S2), indicating that product release and substrate binding does not require trimer dissociation.

Similar structures

A search for structures with similar fold and connectivity as Svi3-3 using PDBeFold (Krissinel and Henrick, 2004) showed that bacterial PII signaling proteins and cation tolerance proteins of CutA type (belonging to a PII-like family) in the GlnB-like superfamily have similar trimeric architectures of ferredoxin-like folds. The closest structural neighbors superpose with RMSDs above 2 Å over no more than 86 C_α atoms. PII regulatory proteins bind ATP/ADP and 2-oxoglutarate at the trimer interface, and conformational changes of loops in response to ligand binding and modification modulates binding to other proteins (Forchhammer and Lüddecke, 2016). Intriguingly, the position of ATP is similar to where SAH binds to Svi3-3, although the binding site appears non-conserved.

Catalytic residues

The reaction mechanism of the presumed SAM hydrolases (Fig. 1) is previously unexplored. Two possibilities would either be that the enzyme provides a catalytic base that by deprotonation activates a water molecule for nucleophilic attack on the γ carbon of SAM, or that a catalytic residue from the enzyme acts as nucleophile and attacks the γ carbon, forming a covalent intermediate with the substrate that subsequently gets hydrolyzed by reaction with a water molecule. In both scenarios, a catalytic amino acid in proximity to the site of hydrolysis would be needed.

Inspection of the active site shows that Glu69 is relatively close to the site of cleavage (Fig. 2C), making this residue the most likely candidate. Another possible residue that could

act as a base or a nucleophile is Tyr58, which in such case would need to donate a proton to the nearby Glu105 (Fig. 2C). To test these possibilities, Svi3-3 mutants Y58F, E69Q, E69A and E105Q were constructed, expressed and purified for *in vitro* activity assays. The Y58F mutant eluted mainly as monomer, indicating a de-stabilized trimer, while all other mutants migrated as trimers. The activity of wild type and mutant Svi3-3 variants in conversion of SAM to MTA was determined at 1 mM substrate concentration. The wild type truncated Svi3-3 construct showed an average turnover of 9.5 s^{-1} at 25°C, nearly doubled compared to the full length, His-tagged construct (Jerlström Hultqvist et al., 2018), but with significant deviation between batches (Fig. S3). The mutant enzymes all showed reduced activity compared to wildtype (Fig. 4A, Fig. S3). For the Y58F and E105Q mutants, activity was 5-fold and 3-fold reduced, whereas for the E69Q and E69A mutants, activity was nearly abolished (4500- and 1500-fold reduction). Thus, Glu69 is *in vitro* critical for substrate binding, catalysis or both.

Thermal shift binding assays

To characterize the binding of substrate and product to Svi3-3, thermal unfolding experiments were performed using differential scanning fluorimetry (DSF) (Niesen et al., 2007). In presence of the substrate SAM, its analogue SAH or the reaction product MTA, the melting temperature of the wild type enzyme increased by up to 30°C, demonstrating a major stabilizing effect on the structure (Fig. 4B). Under the assay conditions, the substrate is most likely turned over, and as a result, the sample with SAM is stabilized by binding of MTA. A large stabilization was also seen in thermal denaturation assays followed by circular dichroism in presence of MTA (data not shown).

The DSF assay clearly demonstrates that the E69Q mutant is not impaired in binding of SAM or MTA, but that binding of SAH is abolished (Fig. 4B). However, despite extensive

trials, a structure of Svi3-3 E69Q with SAM could not be obtained. A crystal structure of Svi3-3 E69Q with MTA shows no major conformational changes of the enzyme, but a minor shift of the mutated side chain close to the reaction site (data not shown).

Structure-guided sequence alignment supports conservation of structure and reaction mechanism

A structure-guided multiple sequence alignment of Svi3-3 with T3 SAMase and two other polypeptides annotated with SAM hydrolase activity (Orf1 and Svi3-7 (Jerlström Hultqvist et al., 2018)) but with barely detectable sequence similarity, suggests that a similar core fold can be formed by all aligned enzymes (Fig. 5). Only three amino acids are strictly conserved, and only a handful conservatively substituted. Based on the SAH structure, all the conserved residues are important for binding of SAM. Gly56 packs against the ribose, not allowing space for a side chain, Glu69 and Gln103 as described above form hydrogen bonds to the ligand and Tyr58 packs against the γ carbon and forms a hydrogen bond to Glu104, enclosing the ligand.

The Svi3-3 structure allows interpretation of the effect of loss-of-function mutations identified in the previous complementation studies (Jerlström Hultqvist et al., 2018). One group of disabling mutations would act to sterically disturb the interaction between the monomers and/or change the character of the interface (R14C, V33D, V52D, E110K, G115V). Mutation of the conserved glycine (G56D) would clash with the ribose in MTA and SAH, and thereby disturb substrate binding. The remaining mutations (A13V, A93G, G95D) are likely to affect folding or stability of the structure.

Mutagenesis of catalytic residues in homologous enzymes

To validate the structure-guided sequence alignment, Glu68 in T3 SAMase, predicted by the sequence alignment (Fig. 5) to be the equivalent of Glu69 in Svi3-3, was mutagenized and tested for *in vitro* activity. The E68Q mutant of T3 SAMase retained 20-30% activity compared to WT.

In addition, mutant variants carried on an inducible plasmid were tested for their ability to rescue the *ΔilvA* auxotrophic mutant (Fig. S1) (Jerlström Hultqvist et al., 2018) under uninduced and induced conditions. Wild-type T3 SAMase because of its toxicity at higher expression level only shows rescue under uninduced conditions (Jerlström Hultqvist et al., 2018). Both T3 SAMase and Orf1 contain two consecutive acidic residues (E67 and E68 in T3 SAMase, E50 and D51 in Orf1, Fig. 5), both of which were conservatively mutated. No rescue was observed either for the Svi3-3 E69Q, Svi3-3 E69A, Orf1 E50Q, or the T3 SAMase E68Q mutants, suggesting a loss or reduced activity of these variants (Table S2) and validating the sequence alignment. Mutations of the neighboring acidic residues (E67Q in T3 SAMase and D51N in Orf1) still allowed rescue under the same conditions as the corresponding wild-type.

Given that we observed measurable activity for the T3 SAMase E68Q mutant *in vitro*, we decided to insert different variants of the T3 SAMase on the chromosome, to allow titration of the expression levels. To this end, the different mutant gene variants were placed downstream of the p*BAD* promoter in a *ΔilvA* knockout mutant. Different concentrations of L-arabinose were used to induce the expression of these variants to determine if the variants could show *in vivo* activity at higher expression levels. For the E68Q mutant, growth was only observed at the highest concentration of arabinose (0.1%), where low enzymatic activity can be compensated by increased enzyme levels (Table S3).

Molecular dynamics simulations of Svi3-3 in complex with substrate

To gain further insights into substrate binding to Svi3-3, molecular dynamics (MD) simulations were performed. An initial complex of Svi3-3 with SAM was generated from docking calculations, which indicated a slight binding preference for SAM over SAH. A total of 100 ns of MD simulation was run for both apo and holo Svi3-3. The holo simulation revealed that the SAM conformation in the active site is very stable, particularly the methionine part (Fig. S4). In agreement with the experimental structure with SAH, the carboxylate group is strongly stabilized by the backbone amide hydrogens of Glu105 and Ser106, whereas the amino group is primarily stabilized by the side-chains of Glu69 and Gln104 (Fig. S4A). Moreover, the positively charged methionine S atom is consistently stabilized through a π-cation interaction with the Tyr58 side-chain (Fig. S5A). The adenosine part of SAM is primarily stabilized by H-bond interactions with the side-chain of Ser50 and the backbone of Val57 and Ile77, as illustrated in Figure S4. When comparing the averaged root mean square fluctuations (RMSF) of the protein backbone, Svi3-3 was more flexible throughout the 100 ns MD simulation without SAM in the active site (apo). Here the average RMSF for the entire Svi3-3 trimer is 0.91 $Å^2$ and 0.86 $Å^2$ for the apo and holo, respectively. Interestingly, the residues surrounding the active site cavity, and in particular the methionine stabilizing residues 104 – 106, become significantly more flexible in the apo simulations (Fig. S5B). Thus, 100 ns of MD simulation demonstrated that Svi3-3 is most flexible in the regions surrounding the active site and that these regions become significantly more rigid upon substrate binding.

Computational studies of the SAMase reaction mechanism

The mechanism of enzymatic SAMase activity is previously unexplored. Thus, the observed active site conformations from the MD simulations were used to build a cluster model (Fig. S5C) to investigate the SAMase reaction mechanism with density functional theory (DFT).

The simulations revealed one potential, but not optimally positioned, water molecule for hydrolysis that was stabilized by H-bonds between the backbone of Ser106 and Gln104, but there were no obvious residues within reach to activate this water by acting as a base.

Glu69 was initially suspected to either work as a catalytic base, activating a water molecule for hydrolysis, or as a nucleophile, attacking the γ-carbon of SAM. However, no water molecule was observed with a suitable position with respect to Glu69 in the experimental structures or after the MD simulation, indicating that the role as a catalytic base is unlikely. Moreover, the observed SAM configuration relative to Glu69 was not optimal for attack on the γ-carbon of SAM. DFT geometry optimizations furthermore failed to locate any stationary point (transition state) for the attack, suggesting that the role as a nucleophile is also unlikely. Thus, it seems that the main role of Glu69 is to bind and orient the substrate in the active site by accepting H-bonds primarily from the amino group of SAM, but also from the 3'-hydroxyl group of the ribose ring (Fig. S5C). In fact, the only residue in the active site oriented properly for a potential hydrolase reaction mechanism is Tyr58. However, DFT calculations could exclude the possibility of Tyr58 acting as a nucleophile in such a mechanism.

Further DFT geometry optimization, however, revealed a completely different mechanism, a unimolecular reaction resulting in the formation of homoserine lactone (Fig. 6A). The DFT optimized stationary points shown in Figure 6A indicate that Tyr58 is deprotonated and bridged by a water molecule to the protonated Glu105. Deprotonation of Tyr58 enhances its cation-π interaction with the S atom of SAM and the electrostatic preorganization weakens the bond to the ribose ring. Together with the amino group interaction with Glu69 this makes the configuration of SAM in the active site of Svi3-3 susceptible to intramolecular carboxylate oxygen attack on the γ-carbon. The activation energy for the formation of homoserine lactone in the DFT cluster model was calculated to be

16.8 kcal/mol with an exothermic reaction energy of –5.7 kcal/mol (Fig 6B). Interestingly, in the product state (Fig 6A), Glu69 shares a proton with the SAM amino group and the water molecule also makes a short strong hydrogen bond with Tyr58. This water appeared to be a good candidate for nucleophilic attack on the carbonyl carbon of homoserine lactone, thereby forming a tetrahedral intermediate which could break down to homoserine. The calculated barrier for this step is 17.5 kcal/mol, which is not unrealistically high, but the reaction energy for the tetrahedral intermediate is 25.2 kcal/mol relative to the homoserine lactone (Fig. 6B). Thus, the DFT calculations indicate that Svi3-3 forms homoserine lactone, but that further breakdown to homoserine does not occur in the active site.

Most importantly, the DFT calculations clearly predict that Svi3-3 is not a SAM hydrolase, but rather a SAM lyase, catalyzing the unimolecular transformation of SAM to homoserine lactone, whereafter this product is released from the active site.

The carboxyl group of SAM appears essential for MTA production

One prediction from the suggested reaction mechanism is that the carboxyl group of SAM is essential for the degradation of SAM by Svi3-3. To test this hypothesis, decarboxylated SAM (dcSAM) was produced enzymatically from SAM using SAM decarboxylase (Cohn et al., 1983) and used as a substrate in the MTA formation assay. In support of the proposed mechanism, we observed no Svi3-3-catalysed production of MTA from dcSAM (Fig. S6). In DSF binding assays, dcSAM does not induce a thermal stabilization of Svi3-3, indicating that the carboxyl group is important for binding and/or stabilization of the structure.

Experimental verification of reaction products by thin-layer chromatography and NMR spectroscopy

Our activity assay (Jerlström Hultqvist et al., 2018) is based on detection of MTA that is also observed in the structure from co-crystallization of Svi3-3 with SAM. Thus, MTA is indeed formed in the reaction. In order to test the predictions from the DFT calculations, we used thin-layer chromatography (TLC), commonly used for separation of amino acids, to determine whether homoserine was formed. The substrate SAM and the products could be separated by TLC, the adenosyl-containing compounds were visualized under UV light and the amines were stained with ninhydrin after pre-treatment with β-mercapto ethanol (BME). Interestingly, we observed a reaction product with mobility and color upon staining distinct from homoserine, proving that Svi3-3 is not a SAM hydrolase. The same assay was performed with T3 SAMase and Orf1 and comparison with reference samples shows that for all three enzymes, a reaction product is observed that on TLC migrates and stains similarly to homoserine lactone (Fig. 7A), supporting the hypothesis that Svi3-3, T3 SAMase and Orf1 are indeed SAM lyases.

To confirm the identity of the reaction product, the enzymatic reaction products were examined with ^{1}H NMR and the spectrum compared to reference spectra for SAM, homoserine and homoserine lactone (Fig. 7B, S7). The results confirm that homoserine lactone is formed on the same time scale as MTA. Upon incubation of homoserine lactone in phosphate buffer at pH 7.4, the lactone is transformed to homoserine through spontaneous hydrolysis (Fig. S8).

Discussion

Relation to other enzymes with similar activity and structure

Svi3-3 represents the first structure of a phage-encoded SAM degrading enzyme. There is no previously established reaction mechanism for these enzymes, and to our knowledge there are only two previous examples of enzymes that can cleave a trialkyl sulfonium substrate. A

distinct type of SAM lyase, 1-aminocyclopropane-1-carboxylate synthase (ACC synthase, EC 4.4.1.14) exists in higher plants and some fungi. The products of this enzyme are MTA and 1-aminocyclopropane-1-carboxylate that is used in the biosynthetic pathway for ethylene. The reaction is PLP-dependent and the enzyme is structurally and mechanistically unrelated to the phage encoded SAM lyases (Capitani et al., 1999).

Instead, Svi3-3 shows structural similarity to PII and PII-like proteins, many of which bind nucleotides or nucleotide-derived metabolites in the inter-subunit clefts. Despite very low levels of sequence identity within those families, they have been suggested to have arisen by divergent evolution from a common ancestor (Forchhammer and Lüddecke, 2016). Based on this similarity, we tested binding of ATP, ADP and AMP to Svi3-3 by DSF, but detected no interaction. Still, these two families of enzymes may have a distant evolutionary relationship.

Substrate binding

Svi3-3 forms a trimer in solution both in absence and in presence of substrate (Fig. S2). Thermal shift binding experiments showed a major stabilization of Svi3-3 upon binding of MTA or SAH (Fig. 4B). Comparisons of the apo and ligand-bound structures as well as MD simulations indicate that stabilization is caused by ordering of the β7- β8 hairpin and tightening of the trimer around the ligand. Results presented here show that E69 in Svi3-3 plays a critical role in the enzyme, and the failure in getting crystals of an E69Q mutant with SAM suggests that binding of SAM may be associated with conformational changes that are incompatible with crystal packing or with the crystallization conditions. The observation that the E69Q mutant binds SAM but does not bind SAH indicates that although SAH only lacks one methyl group compared to SAM, the complex structure of wildtype Svi3-3 with SAH may not fully mimic the substrate-bound state. Since MTA and SAH show a perfect overlap

between the two structures (Fig. 2D), any such difference in binding mode between SAM and SAH is likely to involve the methionine end of the substrate, where MD indicates that Tyr58 forms a cation-π interaction with the positively charged sulfur. The reason for why the E69Q mutant does not bind to SAH may be that two important interactions are lacking; Q69 cannot accept two hydrogen bonds (Fig. 2C) and there is no positive charge on the sulfur that can participate in the cation-π interaction with Tyr58.

Phage-encoded SAMases are lyases

Prompted by DFT calculations producing high energy barriers for a hydrolysis reaction within the active site of Svi3-3, the TLC assays and NMR show unambiguously that Svi3-3 is a SAM lyase forming homoserine lactone and MTA (Fig. 7). The lactone is spontaneously converted to homoserine in solution (Wu et al., 1983) (Fig. S8, 8). Previous attempts to set up a coupled SAM hydrolase activity assay for Svi3-3 using homoserine dehydrogenase or homoserine kinase failed to show homoserine production with the same rate as MTA production (data not shown). The observed rates were 1000-fold lower, and we can now explain that this is due to the slow and un-catalyzed formation of homoserine from the homoserine lactone that is enzymatically formed.

Computational work by others suggests that the non-enzymatic degradation of SAM to homoserine lactone and MTA is slowed down by the favorable interactions of the carboxylate group with water (Lankau et al., 2017). Thus, Svi3-3 increases the reactivity of the carboxylate group by excluding water from the corresponding part of the active site, while stabilizing a reactive conformation of the substrate. For this unimolecular reaction mechanism (Fig. 8A), only very few strictly conserved residues are required, as illustrated in the multiple-sequence alignment (Fig. 5). Both hydrogen bond acceptors of Glu69 seem critical for stabilization of the reactive state (Fig. 8), and Svi3-3 E69Q has nearly abolished activity.

However, the effect of the corresponding mutation in T3 SAMase is not quite as dramatic. Since the level of sequence identity between the two enzymes is low, there will be many differences in the active site, and additional interactions may contribute to stabilizing the reactive state for the same mechanism in T3 SAMase.

The only previously partly characterized phage SAMase comes from phage T3. It was identified based on its anti-restriction activity, but the mechanism was never fully clarified. Anti-restriction activity of the closely related T7 phage is based on the OCR protein that forms a structure that mimics B-form DNA and blocks DNA binding of EcoKI and other type I RM systems (Walkinshaw et al., 2002). The first structure from the SAM lyase enzyme family that we present here clearly proves that they have no structural similarity to the OCR protein. Instead, our data shows that also the T3 SAMase is a lyase and not a hydrolase, but future studies are needed to elucidate whether these enzymes also have additional mechanisms of anti-restriction activity (Spoerel et al., 1979).

Around the same time as the SAM-degrading enzyme from bacteriophage T3 was discovered, the same enzymatic activity was also found in extract from bacteria (Shapiro and Mather, 1958) and yeast (S. Mudd, 1959; S. H. Mudd, 1959). In both of these systems, the reaction products were described as MTA and γ-aminobutyro-lactone (homoserine lactone), and the conversion to homoserine was considered to be spontaneous. In contrast, the phage enzyme from T3 was early described as a SAM hydrolase, and referred to as such until this day. In the early literature, homoserine lactone was identified as an intermediate (Gold et al., 1964) but, perhaps due to the available methods at the time, it was not realized that homoserine was formed on a different time-scale from MTA, indicating a spontaneous and not enzyme-catalyzed reaction. For this reason, it is not until now that we can correct the functional annotation to SAM lyase.

411 The SAM lyases show very low sequence conservation and large variations in size
412 (Fig. 5), and future studies will elucidate the relationship between structure and activity in this
413 family of enzymes, their prevalence and their exact biological roles in different organisms.
414
415 **Methods**
416 ***Cloning***
417 For expression of an N-terminally truncated construct of Svi3-3, the *svi3-3* gene was PCR
418 amplified using Pfu DNA polymerase with primers Svi3-3_d19f and Svi3-3_r1 and cloned
419 into the pEXP5-NT/TOPO vector (Invitrogen) according to the manufacturers protocol.
420 Transformants were selected on LA plates supplemented with 100 µg/ml ampicillin. The
421 correctness of plasmid pEXP5-Svi3-3_d19 was confirmed by sequencing (Eurofins). The
422 resulting plasmid encoded amino acid 20-162 of the original His-tagged Svi3-3 polypeptide
423 (corresponding to residue 5-147 from the phage-encoded sequence) fused to an N-terminal
424 hexahistidine tag followed by a TEV cleavage site. The sequence is numbered starting at the
425 N terminus of the TEV-cleaved protein sequence, corresponding to an offset of -16 in relation
426 to previous work (Jerlström Hultqvist et al., 2018).
427
428 ***Site-directed mutagenesis***
429 Svi3-3-d19 mutants Y58F, E69Q, E69A and E105Q were generated by site directed
430 mutagenesis of pEXP5-Svi3-3_d19 using the QuickChange II protocol (Stratagene) using the
431 primers listed in Table S4. Mutations were confirmed by DNA sequencing.
432
433 ***Protein expression and purification***
434 Expression plasmids were transformed into BL21-AI cells and plated on LA plates containing
435 50 µg/ml ampicillin and 0.1% glucose. For protein expression, 5 ml overnight culture in LB

containing 50 µg/ml ampicillin and 0.1% glucose was used to inoculate 800 ml LB medium with the same composition and incubated at 37°C with shaking. When OD_{600} reached 0.9, expression was induced with 0.2% L-arabinose and the culture was further incubated at 37°C for 4 hours before harvest by centrifugation. The cell pellet was resuspended in buffer A (50 mM Tris-HCl pH 7.5, 300 mM NaCl, 20 mM imidazole, 5 mM BME) including cOmplete EDTA-free protease inhibitor (Roche) and subjected to lysis by sonication. After centrifugation at 30,000 x g for 30 min, the supernatant lysate was clarified by filtration through a 0.45-µm-syringe filter, loaded to a gravity column containing pre-equilibrated Ni-Sepharose (GE Healthcare) and incubated under slow rotation for 10 min at 4 °C. The column was washed extensively with buffer A supplemented with 20mM imidazole, and the His-tagged protein was eluted with buffer A containing 500 mM imidazole. Protein-containing fractions were loaded onto a HiLoad 16/60 Superdex 75 column equilibrated with buffer B (25 mM Tris-HCl, 150 mM NaCl, pH 8.0). Wildtype Svi3-3_d19, E69Q, E69A and E105Q mutants eluted as trimers, while the Y58F mutant eluted mainly as monomer. Peak fractions were pooled and concentrated to 2 mg/ml. To cleave off the His-tag, the protein was incubated at 4°C overnight with a 1:10 molar ratio of TEV_{SH} protease (Van Den Berg et al., 2006). The cleavage reaction was passed through Ni-Sepharose before being loaded onto a HiLoad 16/60 Superdex 75 column equilibrated in buffer B. Peak fractions were concentrated to 10 mg/ml for further use.

T3 SAMase was produced by *in vitro* transcription-translation as previously described (Jerlström Hultqvist et al., 2018).

Crystallization, data collection and structure determination.

Crystallization was done using the sitting-drop vapour diffusion method at room temperature (293 K). Crystals grew in 2-10 days in drops containing 1 µl Svi3-3_d19 (10 mg/ml, with or

without 5 mM SAH/SAM) and 1 µl of reservoir solution containing 0.4-0.6 M ammonium phosphate. Crystals were cryo-protected in reservoir solution supplemented with 1.5 M proline and vitrified in liquid nitrogen for data collection. All data were collected at ESRF beamline ID23-1 at 100K and processed with XDS(Kabsch, 2010). The Svi3-3_d19 structure with SAM was solved with *ab initio* methods using Arcimboldo_lite(Rodríguez et al., 2009) run on the National Supercomputer Center (NSC) in Linköping and a 15 amino acid helix as search model(McCoy et al., 2007). The structure was manually rebuilt in Coot (Emsley et al., 2010) and refined using phenix.refine(Afonine et al., 2012). Statistics for data collection and refinement are summarized in Table 1.

SAXS

SEC-SAXS data for Svi3-3_d19 samples were collected at the Diamond Light Source on beamline B21. In-line SEC-SAXS was performed using an Agilent 1200 HPLC system connected Shodex KW403 column. Data were recorded on a Pilatus 2M detector with a fixed camera length of 4.014 m and 12.4 keV energy allowing the collection of the angular range q between 0.0038–0.42 $Å^{-1}$.

His_6-tagged Svi3-3_d19 samples at 10-13 mg/ml concentration with and without 5 mM SAM were loaded onto the size exclusion column previously equilibrated in 25 mM Tris-HCl pH 8.0, 150 mM NaCl. The data was initially subtracted with the buffer and data processing was performed using ScÅtter (Förster et al., 2010). Further data analysis was performed with Primus (Konarev et al., 2003) and SAXSMoW (Piiadov et al., 2019).

Activity assay

The activity of wildtype and mutant versions of the N-terminally truncated Svi3-3 construct was determined according to the previously published discontinuous assay (Jerlström

Hultqvist et al., 2018), by separation of SAM and MTA using cation exchange chromatography. All experiments were conducted at 25°C and the enzyme concentration and duration of the experiment were adjusted to the level of activity, ranging from 50 to 500 nM enzyme and 10 min to 1-week incubation. The experiments were done in biological duplicates (two separately purified batches of each protein) and technical duplicates (two independently pipetted and measured enzymatic reactions).

Differential scanning fluorimetry

The protocol was adopted from Niesen et al.(Niesen et al., 2007). Each 25 µl reaction consisted of 20 µM wild type or mutant Svi3-3 in 25 mM HEPES (4-2-hydroxyethyl- 1-piperazineethanesulfonic acid), 150 mM NaCl, 0.2 µl 50x SYPRO orange dye and 0 - 2500 µM of SAM or SAH. Reactions were done in technical triplicates in a BioRad CFx connect real-time system and subjected to a temperature gradient from 15 °C to 95 °C with an increment of 0.2 °C per 30 s.

Structure-guided sequence alignment

Structure-guided sequence alignment was performed with PROMALS3D (Pei et al., 2008) and manually edited. The sequence alignment figure was prepared using ESPript(Gouet et al., 2003).

Inserting different gene variants encoding T3 SAMases on the chromosome

The different gene variants encoding the wild type and mutant T3 SAMase were inserted on the chromosome of an *ΔilvA* auxotrophic mutant of *E.coli* K-12 MG1655 by λ- red recombineering as previously described (Datsenko and Wanner, 2000). Each of the variants was used to replace the *araBAD* operon, so that the expression for these was under the control

of the p*BAD*, the native promoter for the *araBAD* operon. Briefly, the first step involved replacing the *araBAD* operon in an *ΔilvA E. coli* K-12 MG1655 strain by *cat-sacB-yfp* cassette. The cassette was PCR amplified using the primers araBAD_cat_sacB_F and araBAD_cat_sacB_R (Table S4). Native T3 SAMase, and variants with mutations at E67Q and E68Q were PCR amplified using specific primers that contained homologies surrounding the *araBAD* operon at the 5' end followed by sequences that allowed amplification of the T3 SAMase variants from the respective plasmids (ara_t3samF, ara_t3samR). PCR products were purified, DNA was transformed into the strain containing the *cat-sacB-yfp* cassette at the *araBAD* location, and transformants were selected on sucrose plates. Variants were confirmed by Sanger sequencing (using test_primer_F, test_primer_R, Table S4).

In vivo complementation of ΔilvA mutant with different variants of Svi3-3, Orf1 and T3 SAM hydrolase variants

Two different approaches were used to determine if the different variants of Svi3-3, Orf1 and T3 SAMase could complement the *ΔilvA* auxotrophic mutant. In cases where the variant was present on a plasmid, the plasmid was transformed into the *ΔilvA* auxotrophic mutant and was selected on LA- ampicillin (50 µg/ml) or LA-chloramphenicol (15 µg/ml) plates. The transformants were then re-streaked, and the re-streaked colonies were tested for growth on M9-Glucose (0.2%) minimal media plates, with or without IPTG. On each test plate, the *ΔilvA* auxotrophic mutant containing the empty vector was used as a negative control.

The same approach was used to test functionality of the T3 SAMase variants that were present on the chromosome, with induction being obtained using different concentrations of L-arabinose (0%, 0.01%, 0.05% and 0.1%).

In vivo rescue assay

536 E69A and E69Q variants were constructed for full-length Svi3-3 and Svi3-3_d19 to test for
537 their ability to rescue the *ΔilvA* mutant (Jerlström Hultqvist et al., 2018). Synthetic genes
538 (Eurofins) containing the desired mutations and *Kpn*1 and *Xba*1 cleavage sites were cleaved-
539 out of the original vector and ligated into a modified version of the pCA24N plasmid, purified
540 on a spin-column and transformed directly into the *ΔilvA* mutant. Plasmids were extracted
541 from isolated colonies and sequenced to confirm the correct sequence. The respective clones
542 were then checked for their ability to grow on minimal glucose plates. All *in vivo*
543 complementation experiments were done in biological duplicates.
544
545 ***Molecular Dynamics***
546 Molecular dynamics (MD) simulations of the SAM hydrolase trimer with (holo) and without
547 substrates (apo) in the active sites were performed with Desmond (Bowers et al., 2006;
548 Schrödinger, 2018) using the OPLS3 force field (Harder et al., 2016; Jorgensen et al., 1996;
549 Jorgensen and Tirado-Rives, 1988; Shivakumar et al., 2010). The Svi3-3 crystal structure in
550 complex with SAH was used as starting conformation for the simulations. In the apo
551 simulations the native substrate, S-adenosyl-methionine (SAM), was docked to the active site
552 using Glide (Friesner et al., 2006, 2004; Halgren et al., 2004; Schrödinger, 2018). The
553 docking grid was generated with the OPLS3 force field centered on the S-adenosyl
554 homocysteine (SAH) inhibitor bound to the active site of the Svi3-3 crystal structure. The
555 maestro system builder (Schrödinger, n.d.) was used to solvate the SAM hydrolase trimer
556 with TIP3P (Jorgensen et al., 1983) water molecules in an orthorhombic box with buffer
557 distances of 10 Å to the boundary on all sides. The system was neutralized by addition of Na+
558 ions and the final simulation box consisted of 60972 atoms. A total of 100 ns MD simulation
559 at 298 K was run in the NPT ensemble using the reference system propagator algorithm
560 (RESPA) time stepping scheme (Tuckerman et al., 1991) with time steps of 2 fs for bonded

561 terms, 2 fs for van der Waals and short-range electrostatic interactions and 6 fs for long-range
562 electrostatic interactions. Short range Coulomb interactions were treated with a cutoff radius
563 of 9 Å. Long-range interactions were treated with the smooth Particle Mesh Ewald method
564 (Darden et al., 1993) with a tolerance of 10−9. The NPT ensemble was calculated with the
565 Nose-Hoover chain thermostat method (Hoover, 1985; Nosé, 2002), using a relaxation time of
566 1 ps, and the Martyna-Tobias-Klein barostat method (Martyna et al., 1994), using isotropic
567 coupling with a relaxation time of 2 ps.
568
569 ***Computational reaction mechanism investigations***
570 The catalytic mechanism in SAM was investigated with density functional theory (DFT)
571 calculations. A cluster model (Fig. 5A) was generated from a snapshot of the equilibrated
572 Svi3-3 X-ray structure taken from the MD simulation described above. The active site model
573 was composed of the backbone atoms of Val17, Gly18, Leu19, Asn20 and Val21 chopped at
574 the N- and C-terminal, Tyr58 and Glu69 chopped at the CA position and Gln104, Glu105 and
575 Ser106 (with backbone) chopped at the N- and C-terminals. A smaller substrate mimicking S-
576 adenosyl methionine (SAM) was used for the DFT calculations. Here adenosine was deleted
577 from SAM, resulting in 2-ammonio-4-((R)-ethyl(methyl)sulfonio)butanoate, or S-
578 ethylmethionine (SEM). In addition, a total of 6 water molecules from the MD snapshot were
579 included in the cluster model. To account for the steric effect of the surrounding parts of the
580 protein, atoms in the chopped positions were kept fixed to their original positions (Fig. 5A).
581 The final model after addition of methyl groups to the chopped protein positions consisted of
582 194 atoms (716 electrons).
583 All DFT calculations were performed using the Gaussian 09 (Frisch et al., 2009)
584 package. Geometry optimizations and frequency calculations were computed with the B3LYP
585 functional (Becke, 1993) and the 6-31G(d,p) basis set. Dispersion effects were included in all

586 calculations using Grimme's B3LYP-D3 method (Grimme et al., 2011, 2010). Intrinsic
587 reaction coordinate calculations were performed in both directions from the transition state to
588 verify that the correct minima are connected. Solvent effects were obtained by single-point
589 calculations on the optimized stationary points with the solvent model based on density
590 (SMD) (Marenich et al., 2009). Electronic energies were calculated from single- point
591 calculations on the optimized geometries (RS, TS and PS) at the b3lyp/6-311G+(2d,2p) level
592 of theory. The final reported energies are the electronic energies with the large basis set
593 corrected for zero-point energies (ZPE) and solvent effects in kcal/mol.
594
595 ***Production of SAM decarboxylase***
596 Cells from the ASKA library encoding the SAM decarboxylase (SDC) enzyme were
597 inoculated in LB containing 34 µg/ml chloramphenicol. 5 ml of saturated culture was used to
598 inoculate 800 ml LB medium with the same composition and incubated at 37 °C until OD_{600}
599 reached 0.6. Expression was induced with 0.5 mM IPTG and the culture was incubated
600 overnight at 20 °C. The cells were harvested by centrifugation at 4 °C. The pellet was washed
601 in 25 mM Tris pH 8, 150 mM NaCl, and pelleted again at 8 °C. The cells were resuspended in
602 buffer A (50 mM Tris-HCl pH 8, 300 mM NaCl, 10 mM $MgSO_4$, 5 mM BME) including
603 cOmplete EDTA-free protease inhibitor (Roche) and subjected to lysis by sonication. After
604 centrifugation at 30,000 x g for 30 min, the supernatant was clarified by filtration through a
605 0.45-µm-syringe filter, loaded in a gravity column containing 2 mL of pre-equilibrated Ni-
606 sepharose (GE Healthcare), and incubated under slow rotation for 30 min at 8 °C. The column
607 was washed extensively with buffer A supplemented with 20 mM imidazole, and the His-
608 tagged protein was eluted with buffer A containing 500 mM imidazole. Protein-containing
609 fractions were loaded onto a HiLoad 16/60 Superdex 200 column previously equilibrated with

610 buffer B (25 mM Tris-HCl pH 8, 150 mM NaCl, 10 mM $MgSO_4$, 5 mM BME). Peak fractions
611 were pooled and concentrated to 5 mg/ml.
612
613 ***SAM decarboxylation***
614 0.5 mM SAM was incubated with 20 µM SDC for 2 hours at 37 °C in reaction buffer (20 mM
615 HEPES pH 7, 50 mM KCl, 10 mM $MgSO_4$). After the incubation, 40 µL of the reaction was
616 quenched with the same volume of quenching buffer (50 mM citrate pH 2.6). The rest of the
617 reaction was filtered through a 3 kDa cutoff concentrator to remove the enzyme. The flow-
618 through was collected and dcSAM concentration was determined by the absorbance at 260
619 nm. The fraction of dcSAM was determined using ion exchange chromatography.
620
621 ***dcSAM assay***
622 0.32 mM dcSAM mix (72% dcSAM) was incubated with 0.1 µM Svi3-3 in reaction buffer at
623 37 °C. As a control, dcSAM without Svi3-3 was incubated for the same time. SAM (0.32
624 mM) was incubated with 0.1 µM Svi3-3 and as a control only SAM (0.32 mM) was incubated
625 for the same period of time. Samples of 40 µL were quenched with the same volume of
626 quenching buffer after 0.5 and 23 hours. Samples were analyzed with the same cation
627 exchange method as for the standard activity assay (Jerlström Hultqvist et al., 2018) but using
628 a linear buffer gradient over 7 column volumes.
629
630 ***TLC***
631 For TLC experiments, reactions containing 2 mM SAM and 0.20 µM Svi3-3, 0.20 µM Orf1
632 or 0.25 µM T3 SAMase in 50 mM NaPi pH 7.4 were incubated 20 min at 25°C. MTA
633 product formation of >70% was verified using ion exchange chromatography. 5 x 2ul
634 reaction was loaded on a TLC Silica gel 60 F_{254} plate and developed using a mobile phase of

635 55 % n-butanol, 30 % H_2O, 15 % acetic acid. The plate was treated with BME followed by
636 ninhydrin staining (Basak et al., 2005). Briefly, the dried plate was sprayed with 1 % BME in
637 acetone, heated with a hair dryer, sprayed with 0.25 % ninhydrin in acetone and heated again
638 until spots were clearly visible.
639
640 ***NMR***
641 To analyze reaction products by NMR spectroscopy, a 700 µl reaction mixture was prepared
642 containing 4 mM SAM and 500 nM Svi3-3 d19 in 100 mM Na phosphate buffer pH 7.4 and
643 90% D_2O. The pH of the sample was adjusted to 7.4 after addition of SAM with 5M NaOH.
644 The reaction was incubated for 20 min at 25 °C and shock-frozen in liquid N_2 and stored at -
645 80 °C until measurement. Turnover of >90% of substrate was verified by ion exchange
646 chromatography.
647 ^{1}H NMR spectra were recorded at 600.18 MHz on a Bruker Avance Neo spectrometer
648 equipped with a TCI (CRPHe TR-^{1}H &^{19}F/^{13}C/^{15}N 5mm-EZ) cryogenic probe for samples in
649 aqueous sodium phosphate buffer (NaPi, 100 mM, pH 7.4, solvent D_2O) at 25°C. Typically
650 64 – 128 scans were accumulated with a relaxation delay of 0.7 s and an acquisition time of
651 2.75 s, using the zg30 pulse sequence. Spectra were obtained by zero filling the recorded 32k
652 data points to 128k, followed by multiplication with an exponential weighting function and
653 Fourier transformation.
654 The formation of homoserine lactone in the enzymatic reaction was confirmed by
655 comparison with the ^{1}H NMR spectrum of an authentic sample (from Sigma) dissolved in the
656 same buffer, and by comparison with literature data(Helms et al., 1988). Homoserine lactone
657 spectra were also recorded for various concentrations (70 mM, 17.5 mM, 4.4 mM, 1.1 mM,
658 0.3 mM) and for various times after sample preparation (Fig. S6). The spectra indicated a

659 gradual hydrolysis of the lactone to homoserine that was identified by comparison with
660 literature ^{1}H NMR data (Jamieson et al., 2009) and an authentic homoserine sample.
661
662 **Data availability**
663 The structure coordinates have been deposited to the wwPDB with accession codes 6ZM9
664 (Svi3-3 with MTA), 6ZMG (Svi3-3 with SAH) and 6ZNB (apo Svi3-3). SAXS data has been
665 deposited in SASBDB with accession codes SASDJ65 (Svi3-3 with SAM) and SASDJ55
666 (apo Svi3-3).
667
668 **Acknowledgements**
669 The authors want to thank Ulrika Yngve for advice regarding TLC.
670 This work was supported by grants from the Knut and Alice Wallenberg foundation
671 (Evolution of new genes and proteins) to MS, JÅ and DIA, from the Swedish Research
672 Council grant 2017-03827 to MS, 2017-01527 to DIA and from the Research Council of
673 Norway through a Centre of Excellence and project grants (Grant Nos. 262695 and 274858)
674 to GVI. We are grateful for access to beamlines ID23-1 at the European Synchrotron
675 Radiation Facility (ESRF), Grenoble, France and beamline B21 at the Diamond light source,
676 Didcot, UK. The Archimboldo calculations were performed on resources provided by the
677 Swedish National Infrastructure for Computing (SNIC) at National Supercomputer Centre
678 (NSC) in Linköping. Computational resources for quantum mechanics were awarded by
679 NOTUR; Grant No. nn4654k. This study made use of the NMR Uppsala infrastructure, which
680 is funded by the Department of Chemistry - BMC and the Disciplinary Domain of Medicine
681 and Pharmacy.
682
683

References

Afonine P V., Grosse-Kunstleve RW, Echols N, Headd JJ, Moriarty NW, Mustyakimov M, Terwilliger TC, Urzhumtsev A, Zwart PH, Adams PD. 2012. Towards automated crystallographic structure refinement with phenix. refine. *Acta Crystallogr Sect D Biol Crystallogr* **68**:352–367. doi:10.1107/S0907444912001308

Basak B, Bandyopadhyay D, Patra M, Banerji A, Chatterjee A, Banerji J. 2005. Role of sulfur compounds in the detection of amino acids by ninhydrin on TLC plate. *J Chromatogr Sci* **43**:104–105. doi:10.1093/chromsci/43.2.104

Becke AD. 1993. Density-functional thermochemistry. III. The role of exact exchange. *J Chem Phys*. doi:10.1063/1.464913

Bowers KJ, Chow E, Xu H, Dror RO, Eastwood MP, Gregersen BA, Klepeis JL, Kolossvary I, Moraes MA, Sacerdoti FD, Salmon JK, Shan Y, Shaw DE. 2006. Scalable algorithms for molecular dynamics simulations on commodity clustersProceedings of the 2006 ACM/IEEE Conference on Supercomputing, SC'06. doi:10.1145/1188455.1188544

Capitani G, Hohenester E, Feng L, Storici P, Kirsch JF, Jansonius JN. 1999. Structure of 1-aminocyclopropane-1-carboxylate synthase, a key enzyme in the biosynthesis of the plant hormone ethylene. *J Mol Biol* **294**:745–756. doi:10.1006/jmbi.1999.3255

Cohn MS, Tabor CW, Tabor H. 1983. S-adenosylmethionine decarboxylase of Escherichia coli. *Methods Enzymol* **94**:231–234. doi:10.1016/S0076-6879(83)94040-5

Darden T, York D, Pedersen L. 1993. Particle mesh Ewald: An N·log(N) method for Ewald sums in large systems. *J Chem Phys*. doi:10.1063/1.464397

Datsenko K, Wanner B. 2000. One-step inactivation of chromosomal genes in Escherichia coli K-12 using PCR products. *Proc Natl Acad Sci U S A* **97**:6640–6645. doi:10.1073/pnas.120163297

Emsley P, Lohkamp B, Scott WG, Cowtan K. 2010. Features and development of Coot. *Acta*

709 *Crystallogr Sect D Biol Crystallogr* **66**:486–501. doi:10.1107/S0907444910007493

710 Forchhammer K, Lüddecke J. 2016. Sensory properties of the PIIsignalling protein family.

711 *FEBS J*. doi:10.1111/febs.13584

712 Förster S, Apostol L, Bras W. 2010. Scatter: Software for the analysis of nano-and mesoscale

713 small-angle scattering. *J Appl Crystallogr*. doi:10.1107/S0021889810008289

714 Friesner RA, Banks JL, Murphy RB, Halgren TA, Klicic JJ, Mainz DT, Repasky MP, Knoll

715 EH, Shelley M, Perry JK, Shaw DE, Francis P, Shenkin PS. 2004. Glide: A New

716 Approach for Rapid, Accurate Docking and Scoring. 1. Method and Assessment of

717 Docking Accuracy. *J Med Chem*. doi:10.1021/jm0306430

718 Friesner RA, Murphy RB, Repasky MP, Frye LL, Greenwood JR, Halgren TA, Sanschagrin

719 PC, Mainz DT. 2006. Extra precision glide: Docking and scoring incorporating a model

720 of hydrophobic enclosure for protein-ligand complexes. *J Med Chem*.

721 doi:10.1021/jm051256o

722 Frisch MJ, Trucks GW, Schlegel HB, Scuseria GE, Robb MA, Cheeseman JR, Scalmani G,

723 Barone V, Mennucci B, Petersson GA, Nakatsuji H, Caricato M, Li X, Hratchian HP,

724 Izmaylov AF, Bloino J, Zheng G, Sonnenberg JL, Hada M, Ehara M, Toyota K, Fukuda

725 R, Hasegawa J, Ishida M, Nakajima T, Honda Y, Kitao O, Nakai H, Vreven T,

726 Montgomery JA, Peralta JE, Ogliaro F, Bearpark M, Heyd JJ, Brothers E, Kudin KN,

727 Staroverov VN, Kobayashi R, Normand J, Raghavachari K, Rendell A, Burant JC,

728 Iyengar SS, Tomasi J, Cossi M, Rega N, Millam JM, Klene M, Knox JE, Cross JB,

729 Bakken V, Adamo C, Jaramillo J, Gomperts R, Stratmann RE, Yazyev O, Austin AJ,

730 Cammi R, Pomelli C, Ochterski JW, Martin RL, Morokuma K, Zakrzewski VG, Voth

731 GA, Salvador P, Dannenberg JJ, Dapprich S, Daniels AD, Farkas, Foresman JB, Ortiz J

732 V, Cioslowski J, Fox DJ. 2009. Gaussian 09, Revision B.01. *Gaussian 09, Revis B01,*

733 *Gaussian, Inc, Wallingford CT*.

734 Gefter M, Hausmann R, Gold M, Hurwitz J. 1966. the Enzymatic Methylation of Ribonucleic
735 Acid and Deoxyribonucleic. *J Biol Chem* **241**:1995–2006.
736 Gold M, Hausmann R, Maitra U, Hurwitz J. 1964. Effects of Bacteriophage Infection on the
737 Activity of the Methylating Enzymes. *Proc Natl Acad Sci U S A* **223**:292–297.
738 Gold M, Hurwitz J. 1964. the Enzymatic Methylation of Ribonucleic Acid and
739 Deoxyribonucleic. *J Biol Chem* **239**:3866–3874.
740 Gouet P, Robert X, Courcelle E. 2003. ESPript/ENDscript: Extracting and rendering sequence
741 and 3D information from atomic structures of proteins. *Nucleic Acids Res* **31**:3320–3323.
742 doi:10.1093/nar/gkg556
743 Grimme S, Antony J, Ehrlich S, Krieg H. 2010. A consistent and accurate ab initio
744 parametrization of density functional dispersion correction (DFT-D) for the 94 elements
745 H-Pu. *J Chem Phys*. doi:10.1063/1.3382344
746 Grimme S, Ehrlich S, Goerigk L. 2011. Effect of the damping function in dispersion corrected
747 density functional theory. *J Comput Chem*. doi:10.1002/jcc.21759
748 Halgren TA, Murphy RB, Friesner RA, Beard HS, Frye LL, Pollard WT, Banks JL. 2004.
749 Glide: A New Approach for Rapid, Accurate Docking and Scoring. 2. Enrichment
750 Factors in Database Screening. *J Med Chem*. doi:10.1021/jm030644s
751 Harder E, Damm W, Maple J, Wu C, Reboul M, Xiang JY, Wang L, Lupyan D, Dahlgren
752 MK, Knight JL, Kaus JW, Cerutti DS, Krilov G, Jorgensen WL, Abel R, Friesner RA.
753 2016. OPLS3: A Force Field Providing Broad Coverage of Drug-like Small Molecules
754 and Proteins. *J Chem Theory Comput*. doi:10.1021/acs.jctc.5b00864
755 Hausmann R. 1967. Synthesis of an S-Adenosylmethionine-cleaving Enzyme in T3-infected
756 Escherichia coli and Its Disturbance by Co-infection with Enzymatically Incompetent
757 Bacteriophage. *J Virol* **1**:57–63.
758 Helms GL, Moore RE, Niemczura WP, Patterson GML, Tomer KB, Gross ML. 1988.

759 Scytonemin A, a Novel Calcium Antagonist from a Blue-Green Alga. *J Org Chem*.
760 doi:10.1021/jo00241a033
761 Herrlich P, Schweiger M. 1970. T3 and T7 bacteriophage deoxyribonucleic acid-directed
762 enzyme synthesis in vitro. *J Virol* **6**:750–753.
763 Hoover WG. 1985. Canonical dynamics: Equilibrium phase-space distributions. *Phys Rev A*.
764 doi:10.1103/PhysRevA.31.1695
765 Jamieson AG, Boutard N, Beauregard K, Bodas MS, Ong H, Quiniou C, Chemtob S, Lubell
766 WD. 2009. Positional scanning for peptide secondary structure by systematic solid-phase
767 synthesis of amino lactam peptides. *J Am Chem Soc*. doi:10.1021/ja9010628
768 Janke R, Dodson AE, Rine J. 2015. Metabolism and Epigenetics. *Annu Rev Cell Dev Biol*
769 **31**:473–496. doi:10.1146/annurev-cellbio-100814-125544
770 Jerlström Hultqvist J, Warsi O, Söderholm A, Knopp M, Eckhard U, Vorontsov E, Selmer M,
771 Andersson DI. 2018. A bacteriophage enzyme induces bacterial metabolic perturbation
772 that confers a novel promiscuous function. *Nat Ecol Evol* 1–10. doi:10.1038/s41559-
773 018-0568-5
774 Jorgensen WL, Chandrasekhar J, Madura JD, Impey RW, Klein ML. 1983. Comparison of
775 simple potential functions for simulating liquid water. *J Chem Phys* **79**:926–935.
776 doi:10.1063/1.445869
777 Jorgensen WL, Maxwell DS, Tirado-Rives J. 1996. Development and testing of the OPLS all-
778 atom force field on conformational energetics and properties of organic liquids. *J Am*
779 *Chem Soc* **118**:11225–11236. doi:10.1021/ja9621760
780 Jorgensen WL, Tirado-Rives J. 1988. The OPLS Potential Functions for Proteins. Energy
781 Minimizations for Crystals of Cyclic Peptides and Crambin. *J Am Chem Soc*.
782 doi:10.1021/ja00214a001
783 Kabsch W. 2010. XDS. *Acta Crystallogr Sect D Biol Crystallogr* **66**:125–132.

784 doi:10.1107/S0907444909047337

785 Konarev P V., Volkov V V., Sokolova A V., Koch MHJ, Svergun DI. 2003. PRIMUS: A
786 Windows PC-based system for small-angle scattering data analysis. *J Appl Crystallogr*
787 **36**:1277–1282. doi:10.1107/S0021889803012779

788 Krissinel E, Henrick K. 2004. Secondary-structure matching (SSM), a new tool for fast
789 protein structure alignment in three dimensions. *Acta Crystallogr Sect D Biol*
790 *Crystallogr*. doi:10.1107/S0907444904026460

791 Krueger DH, Presber W, Hansen S, Rosenthal H a. 1975. Biological functions of the
792 bacteriophage T3 SAMase gene. *J Virol* **16**:453–5.

793 Lankau T, Kuo TN, Yu CH. 2017. Computational study of the degradation of S-adenosyl
794 methionine in water. *J Phys Chem A* **121**:505–514. doi:10.1021/acs.jpca.6b09639

795 Loenen WAM. 2006. S-adenosylmethionine: jack of all trades and master of everything?
796 *Biochem Soc Trans* **34**:330–3. doi:10.1042/BST20060330

797 Marenich A V., Cramer CJ, Truhlar DG. 2009. Universal solvation model based on solute
798 electron density and on a continuum model of the solvent defined by the bulk dielectric
799 constant and atomic surface tensions. *J Phys Chem B*. doi:10.1021/jp810292n

800 Martyna GJ, Tobias DJ, Klein ML. 1994. Constant pressure molecular dynamics algorithms. *J*
801 *Chem Phys*. doi:10.1063/1.467468

802 McCoy AJ, Grosse-Kunstleve RW, Adams PD, Winn MD, Storoni LC, Read RJ. 2007.
803 Phaser crystallographic software. *J Appl Crystallogr* **40**:658–674.
804 doi:10.1107/S0021889807021206

805 Mudd S. 1959. The Mechanism of the Enzymatic of S-Adenosylmethionine to a-a-Amino-g-
806 butyrolactone. *J Biol Chem* **234**:1784–1786.

807 Mudd SH. 1959. Enzymatic cleavage of S-adenosylmethionine. *J Biol Chem* **234**:87–92.

808 Niesen FH, Berglund H, Vedadi M. 2007. The use of differential scanning fluorimetry to

809 detect ligand interactions that promote protein stability. *Nat Protoc* **2**:2212–2221.
810 doi:10.1038/nprot.2007.321
811 Nosé S. 2002. A molecular dynamics method for simulations in the canonical ensemble. *Mol*
812 *Phys*. doi:10.1080/00268970110089108
813 Pei J, Kim BH, Grishin N V. 2008. PROMALS3D: A tool for multiple protein sequence and
814 structure alignments. *Nucleic Acids Res* **36**:2295–2300. doi:10.1093/nar/gkn072
815 Piiadov V, Ares de Araújo E, Oliveira Neto M, Craievich AF, Polikarpov I. 2019.
816 SAXSMoW 2.0: Online calculator of the molecular weight of proteins in dilute solution
817 from experimental SAXS data measured on a relative scale. *Protein Sci* **28**:454–463.
818 doi:10.1002/pro.3528
819 Rodríguez DD, Grosse C, Himmel S, González C, de Ilarduya IM, Becker S, Sheldrick GM,
820 Usón I. 2009. Crystallographic ab initio protein structure solution below atomic
821 resolution. *Nat Methods* **6**:651–653. doi:10.1038/nmeth.1365
822 Schrödinger. 2018. Schrödinger Release 2018-1.
823 Schrödinger. n.d. Desmond Molecular Dynamics System.
824 Shapiro SK, Mather AN. 1958. The enzymatic decomposition of S-adenosyl-L-methionine. *J*
825 *Biol Chem* **233**:631–633.
826 Shivakumar D, Williams J, Wu Y, Damm W, Shelley J, Sherman W. 2010. Prediction of
827 absolute solvation free energies using molecular dynamics free energy perturbation and
828 the opls force field. *J Chem Theory Comput*. doi:10.1021/ct900587b
829 Spoerel N, Herrlich P, Bickle TA. 1979. A novel bacteriophage defence mechanism: the anti-
830 restriction protein. *Nature* **278**:30–34.
831 Studier FW, Movva NR. 1976. SAMase gene of bacteriophage T3 is responsible for
832 overcoming host restriction. *J Virol* **19**:136–145.
833 Su X, Wellen KE, Rabinowitz JD. 2016. Metabolic control of methylation and acetylation.

Curr Opin Chem Biol **30**:52–60. doi:10.1016/j.cbpa.2015.10.030

Tuckerman ME, Berne BJ, Rossi A. 1991. Molecular dynamics algorithm for multiple time scales: Systems with disparate masses. *J Chem Phys*. doi:10.1063/1.460004

Van Den Berg S, Löfdahl PÅ, Härd T, Berglund H. 2006. Improved solubility of TEV protease by directed evolution. *J Biotechnol* **121**:291–298. doi:10.1016/j.jbiotec.2005.08.006

Walkinshaw MD, Taylor P, Sturrock SS, Atanasiu C, Berge T, Henderson RM, Edwardson JM, Dryden DTF. 2002. Structure of Ocr from bacteriophage T7, a protein that mimics b-form DNA. *Mol Cell* **9**:187–194. doi:10.1016/S1097-2765(02)00435-5

Weissbach H, Brot N. 1991. Regulation of methionine synthesis in Escherichia coli. *Mol Microbiol*. doi:10.1111/j.1365-2958.1991.tb01905.x

Wilson GG, Murray NE. 1991. Restriction and Modification. *Annu Rev Genet* **25**:585–627. doi:10.1016/B978-0-12-374984-0.01312-7

Wu SE, Huskey WP, Borchardt RT, Schowen RL. 1983. Chiral Instability at Sulfur of S-Adenosylmethionine. *Biochemistry* **22**:2828–2832. doi:10.1021/bi00281a009

Figures & legends

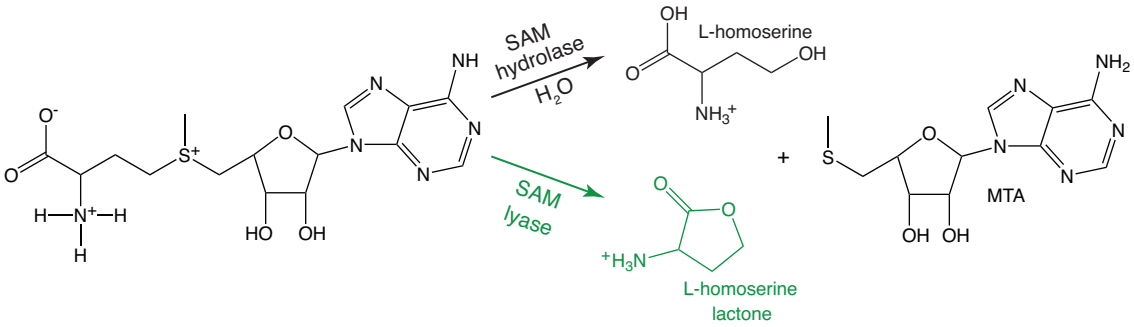

Figure 1. SAMase reaction. Top: Hypothetical SAM hydrolase reaction previously suggested to be catalyzed by T3 SAMase. Bottom, green: SAM lyase reaction shown in this study to be catalysed by all tested bacteriophage SAMases.

857

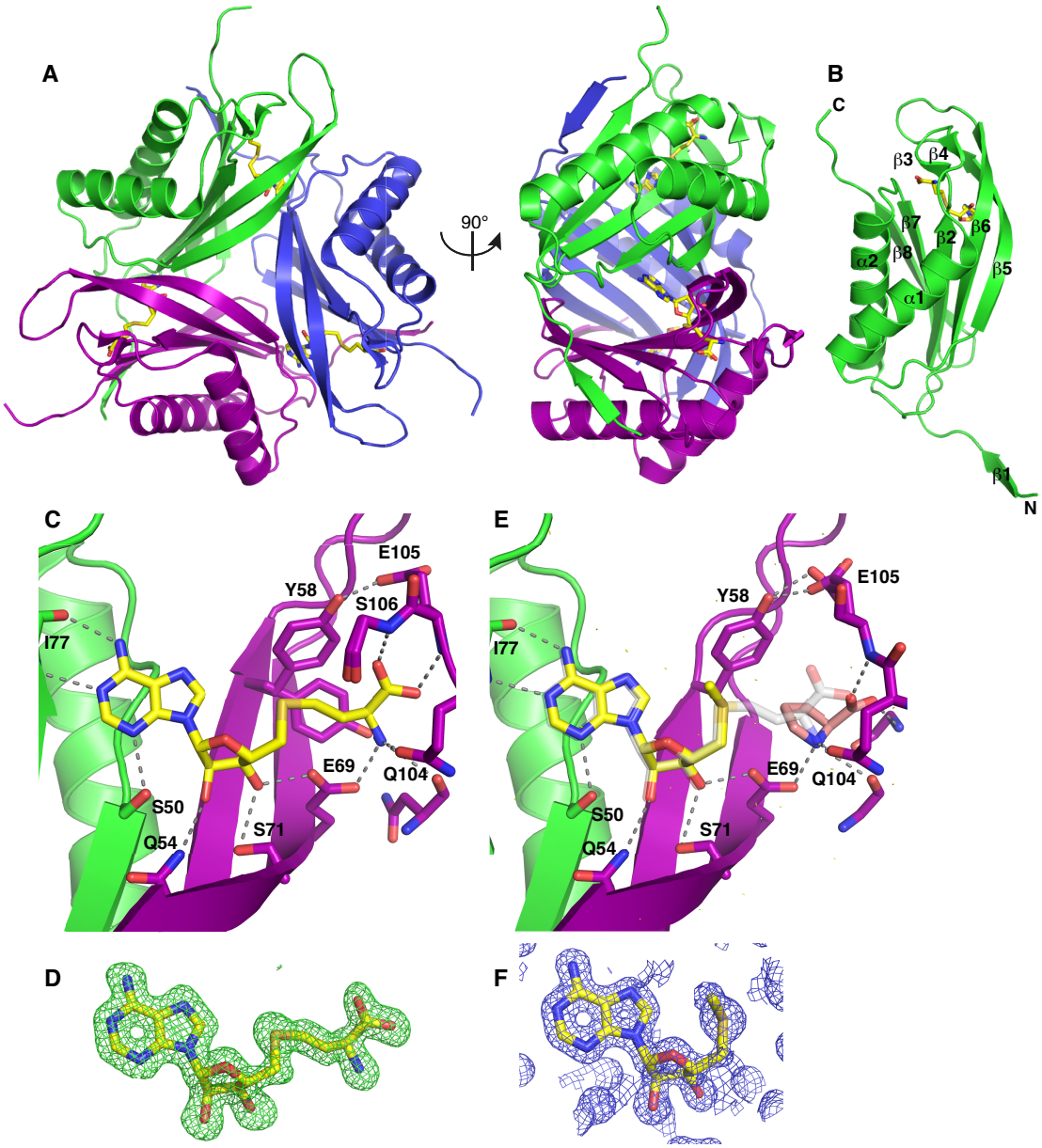

858

859 **Figure 2.** Structure of SAM hydrolase Svi3-3. **A.** Structure of the Svi3-3 trimer in complex
860 with SAH. **B.** Monomer structure of Svi3-3. **C.** Interactions of SAH (yellow sticks) at the
861 trimer interface, **D.** Fo-Fc omit map for SAH contoured at 3 sigma. **E.** MTA (yellow sticks)
862 and Pro (salmon sticks), overlay of SAH is shown in transparent grey sticks. **F.** Unbiased
863 Arcimboldo (Rodríguez et al., 2009) electron density map for MTA bound to Svi3-3,
864 contoured at 2 sigma (0.39 $e^-/Å^3$).

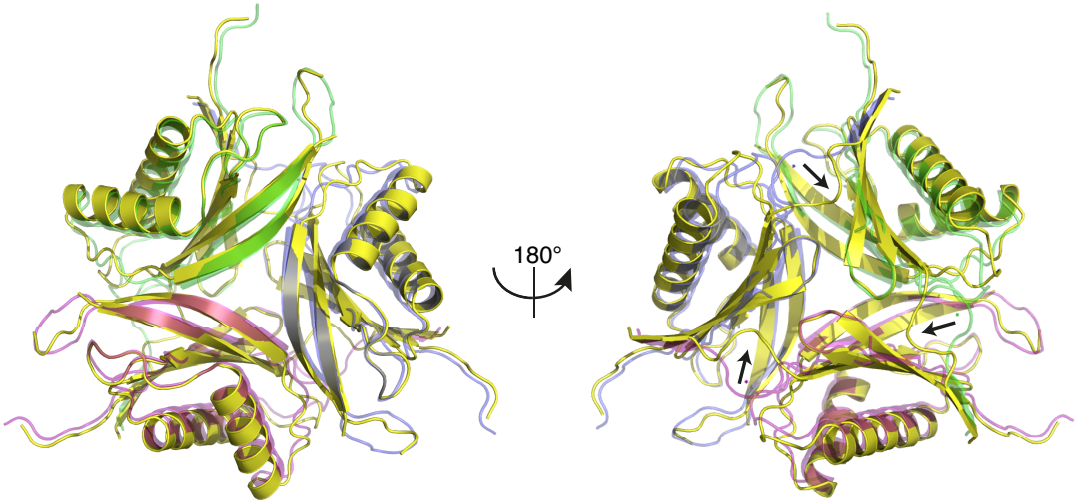

865

866 **Figure 3.** Comparison of the apo structure of Svi3-3 (yellow) and the MTA complex structure

867 (colored as in A, transparent). Arrows indicate conformational differences between the N-

868 terminal regions in the two structures.

869

870

871

872

873

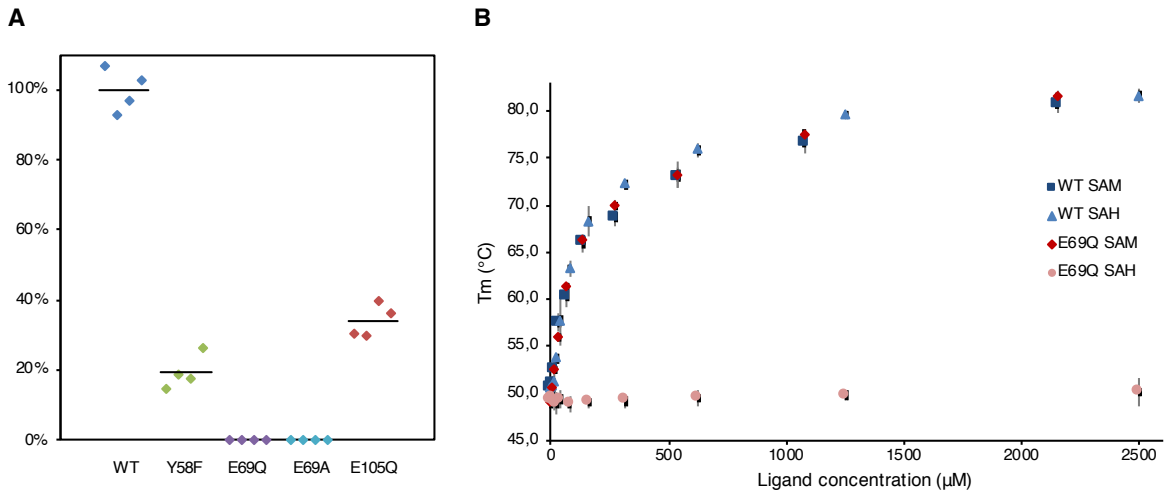

874

875

876 **Figure 4** Svi3-3 assays. **A.** Relative enzymatic activity of Svi3-3 variants. The data points are

877 based on technical duplicates from two different protein purifications, where activity is

878 related to WT purified at the same time. Absolute activity data is presented in figure S3. **B.**

879 DSF data for Svi3-3 variants with different concentrations of SAM and SAH. Error bars

880 correspond to +/- one standard deviation based on triplicate data.

881

882

883

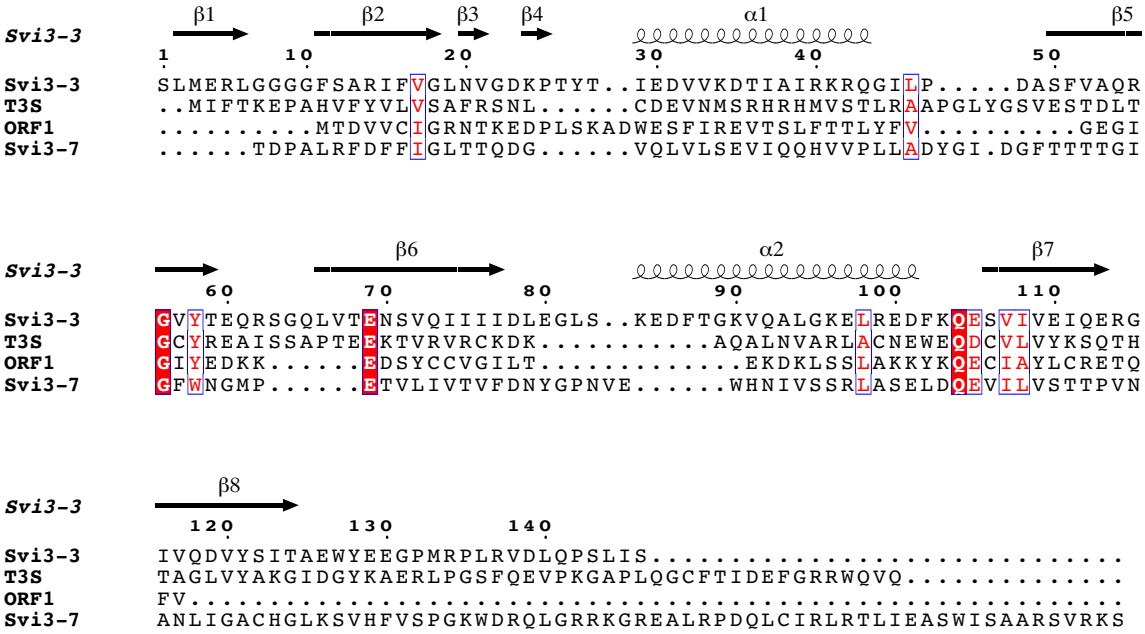

884

885 **Figure 5.** Structure-guided sequence alignment of SAMases with demonstrated activity

886 (Jerlström Hultqvist et al., 2018). Secondary structure of Svi3-3 is displayed above the

887 alignment. Red boxes with white letters indicate conserved residues and red letters in white

888 boxes show conservatively substituted residues. Figure was prepared using ESPript (Gouet et

889 al., 2003).

890

891

892

893

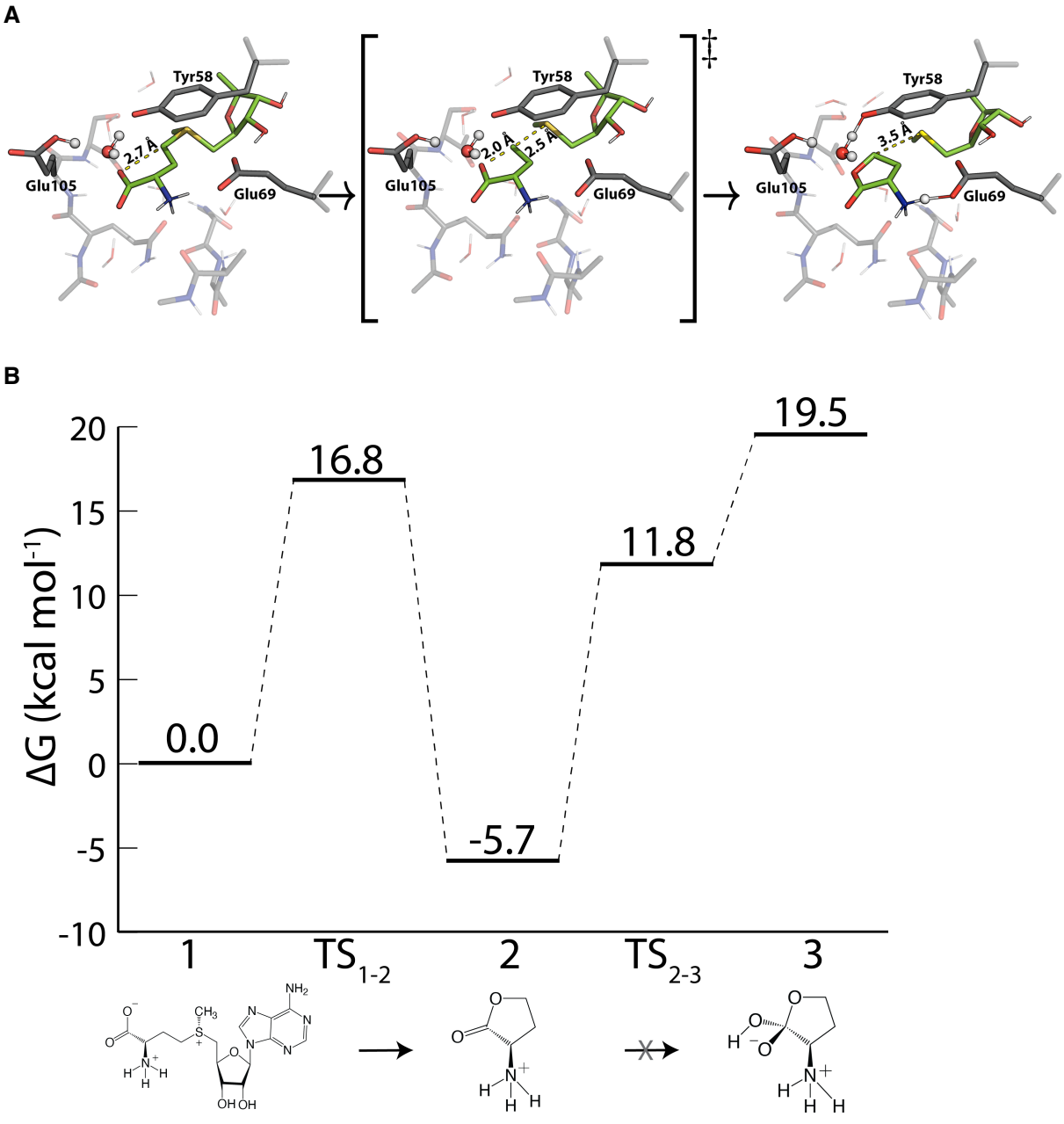

Figure 6. DFT calculations on the SAM lyase reaction of Svi3-3. **A.** Optimized DFT structures for the reactant (left), transition (middle) and product (right) state in the SAM lyase reaction mechanism. **B.** Calculated free energy profiles for reactant (1), transition state (1-2) and product state (2) for the SAM lyase reaction mechanism. Further conversion from homoserine lactone (2) to the tetrahedral intermediate (3) that would form homoserine is not supported by the high DFT energies.

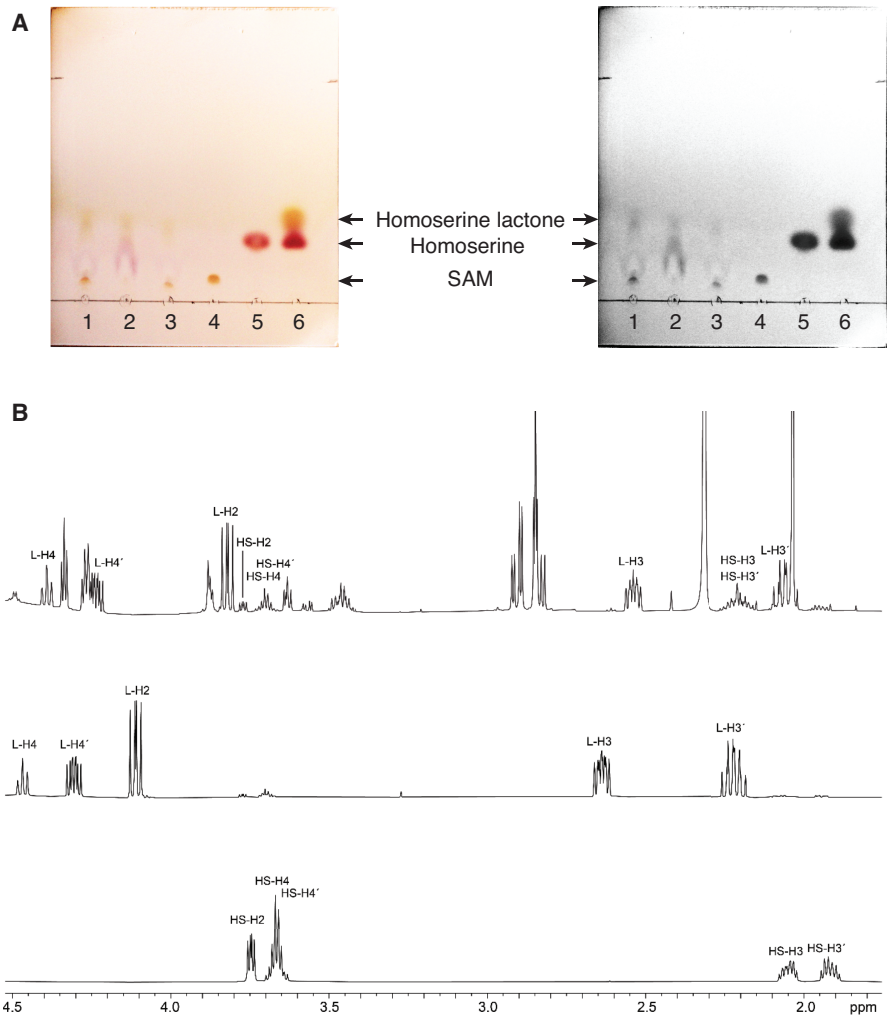

906

907 **Figure 7.** Characterization of SAMase reaction products. **A.** TLC separation of enzymatic
908 reactions and controls, shown in color and gray scale for clarity. (1: Svi3-3, 2: T3 SAMase, 3:
909 Orf1, 4: SAM (17 nmol), 5: L-homoserine (20 nmol), 6: L-homoserine lactone (400 nmol)).
910 **B.** ^{1}H NMR spectra at 600 MHz in sodium phosphate buffer, D_2O, pH 7.4. Top: Enzymatic
911 degradation of SAM (4 mM) (500 nM enzyme) after 45 min. Middle: Homoserine lactone (59
912 mM) showing onset of hydrolysis after 10 min. Bottom: Homoserine (57 mM).

913

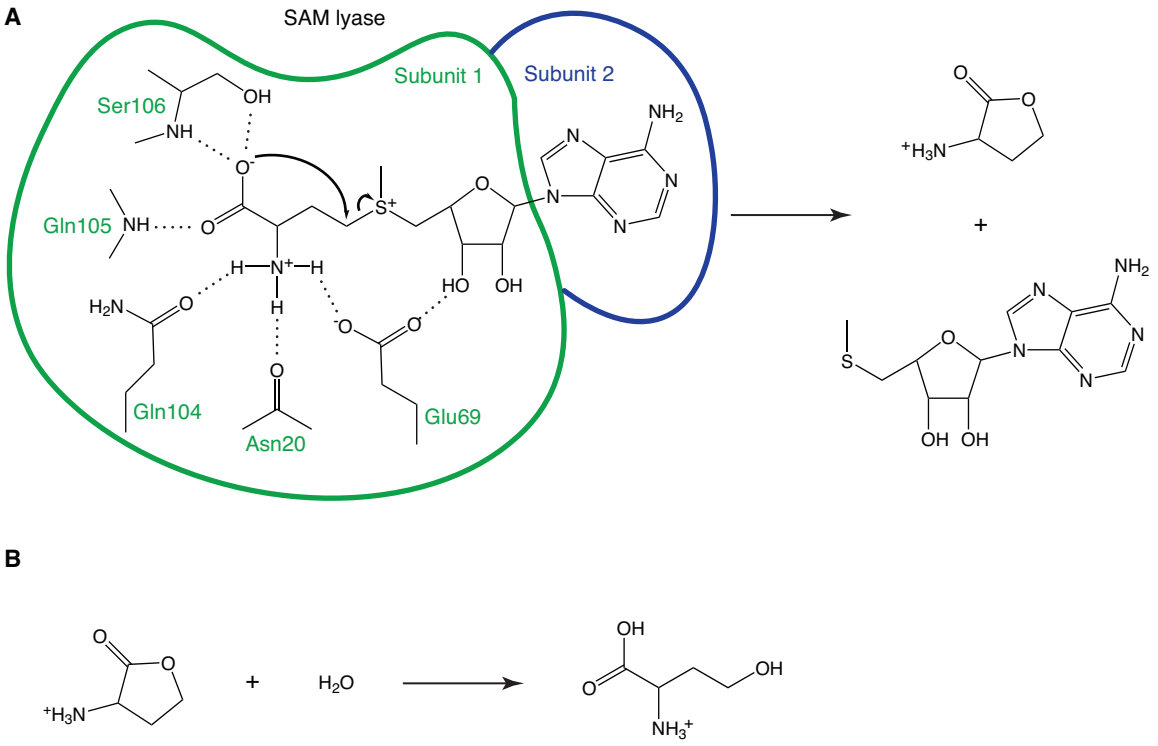

914

915 **Figure 8.** Mechanism of SAM degradation. **A.** The first step is catalyzed by the SAM lyase,

916 releasing the products homoserine lactone and MTA. Hydrogen bonds between the enzyme

917 and the reacting part of SAM are shown as dashed lines. The two subunits contributing to one

918 active site are indicated in green and blue. **B.** Homoserine lactone is spontaneously

919 hydrolyzed to homoserine in solution.

920

921

Tables

Table 1.

	Svi3-3 MTA	Svi3-3 SAH	Svi3-3 apo
Data collection[#]			
Beamline	ID23-1	ID23-1	ID29
Wavelength	0.9184	0.9184	1.0722
Space group	$F4_132$	$F4_132$	$F4_132$
Unit cell parameters:			
a, b, c (Å)	152.3, 154.3, 154.3	154.5, 154.5, 154.5	158.8, 158.8, 158.8
α, β, χ (°)	90, 90, 90	90, 90, 90	90, 90, 90
Resolution (Å)*	46.54-1.45 (1.54-1.45)	44.59-1.48 (1.57-1.48)	39.62-2.8 (2.95-2.80)
R_{meas}(%)*	15.2 (86.2)	12.3 (111.1)	12.5 (93.9)
<I/σ(I)>*	18.8 (3.9)	32.44 (2.04)	9.6 (1.8)
CC ½ (%)*	99.8 (94.8)	100 (77.4)	99.3 (61.0)
Completeness (%)*	99.9 (99.7)	99.7 (98.5)	97.7 (98.5)
Redundancy*	41.3 (40.2)	95.27 (24.9)	5.2 (5.3)
Refinement			
Resolution (Å)	46.54-1.45	44.6-1.48	39.36- 2.8
Reflections / test set	28569/1428	26716/1338	4395/221
R_{work}/R_{free} (%)	13.3/15.5	13.9/17.0	23.2/27.4
Non-hydrogen atoms	1282	1223	992
Protein	1122	1091	979
Ligand/ion	31	10	10
Water	129	122	3
B-factors	22.8	26.0	76.6
Protein	21.8	24.9	76.7
Ligands	14.7	17.4	7.3
Solvent	33.4	36.1	57.8
RMSD from ideal			
bond lengths (Å)	0.008	0.021	0.003
bond angles (°)	1.1	1.8	0.47
Ramachandran plot:			
Preferred (%)	98.4	98.4	95.9
Allowed (%)	0.8	0.8	4.1
Outliers (%)	0.8	0.8	0

* Values within parenthesis refer to the highest resolution shell.

Supplemental material for:

Structure and mechanism of a phage-encoded SAM lyase revises catalytic function of enzyme family

Xiaohu Guo[1,5#], Annika Söderholm[1#], Sandesh Kanchugal P[1#], Geir Villy Isaksen[1,2#], Omar Warsi[3], Ulrich Eckhard[1,6], Silvia Trigüis[1], Adolf Gogoll[4], Jon Jerlström-Hultqvist[3,1], Johan Åqvist[1], Dan I. Andersson[3] & Maria Selmer[1*]

[1] Department of Cell and Molecular Biology, Uppsala University, BMC, Box 596, 751 24 Uppsala, Sweden

[2] Hylleraas Centre for Quantum Molecular Sciences, Department of Chemistry, UiT - The Arctic University of Norway, N9037, Tromsø, Norway.

[3] Department of Medical Biochemistry and Microbiology, Uppsala University, BMC, Box 582, 751 23 Uppsala, Sweden

[4] Department of Chemistry-BMC, Uppsala University, BMC, Box 576, 75123, Uppsala, Sweden

[5] Current affiliation: Division of Biochemistry, Cancer Genomics Center, Netherlands Cancer Institute, Amsterdam, the Netherlands

[6] Current affiliation: Proteolysis Lab, Department of Structural Biology, Molecular Biology Institute of Barcelona, CSIC, Barcelona Science Park, Baldiri Reixac, 15-21, 08028 Barcelona, Catalonia, Spain.

[#] These authors contributed equally to this study.

* to whom correspondence should be addressed: maria.selmer@icm.uu.se

Content:

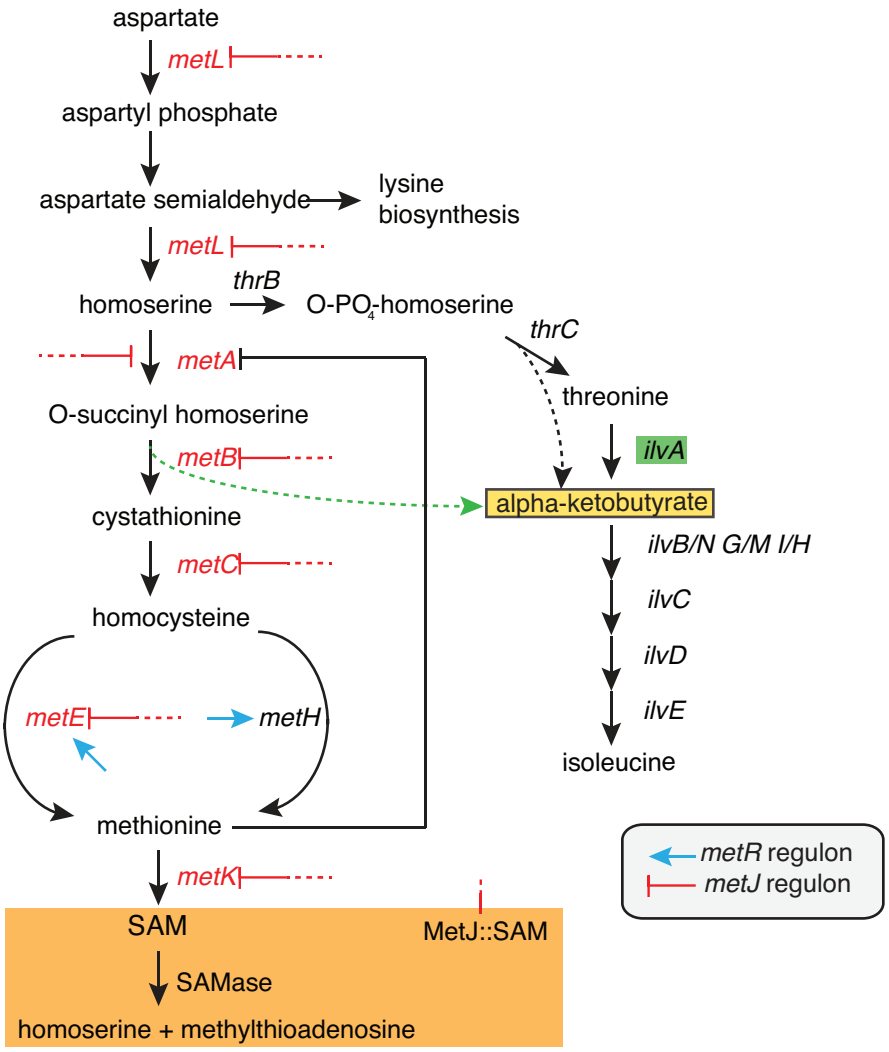

Figure S1. Proposed mechanism of rescue of an *ilvA* auxotrophic mutant by SAMases (Jerlström Hultqvist et al., 2018). Expression of enzymes in the methionine synthesis pathway is repressed by MetJ in complex with SAM. When SAM is degraded by a SAMase, expression increases for the enzymes in the *metJ* regulon. At high expression level, the promiscuous function of MetB, to produce alpha-ketobutyrate from O-succinyl homoserine (green arrow), provides rescue of isoleucine biosynthesis.

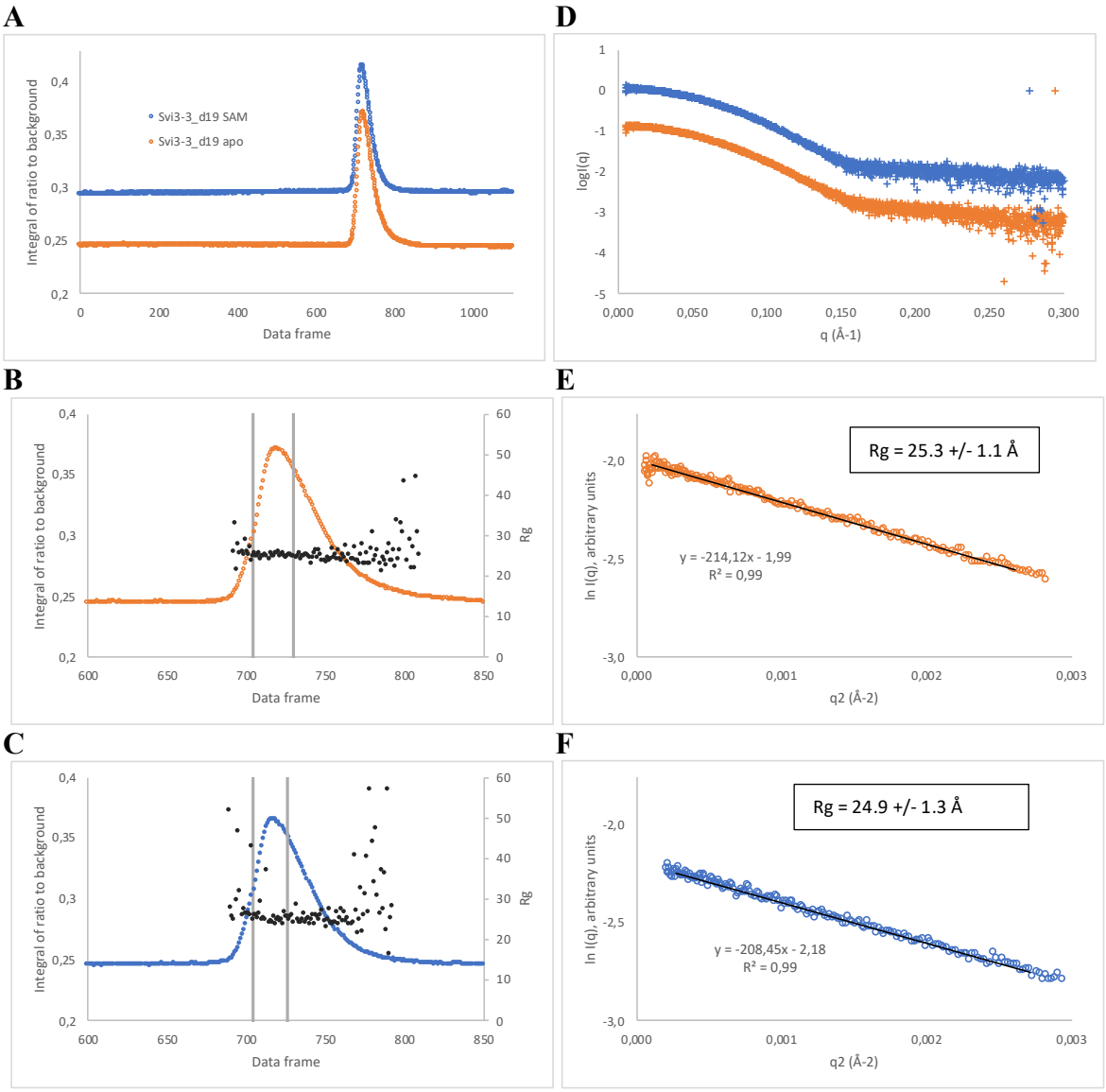

Figure S2. SEC-SAXS of Svi3-3-d19. **A**. Overlay of signal plots from SEC-SAXS of Svi3-3_d19 in presence and absence of 5 mM SAM (plotted with an offset of 0.05 for clarity). **B.** Zoom in of signal plot for Svi3-3_d19 apo. Black markers indicate the radius of gyration calculated from the individual scattering curves. Grey bars indicate the data frames used for further analysis. **C.** Zoom in of signal plot for Svi3-3_d19 in presence of SAM. Black markers indicate the radius of gyration calculated from the individual scattering curves. Grey bars indicate the data frames used for further analysis. **D.** Scattering curves for Svi3-3_d19 in presence and absence of SAM. Colors as in A. The blue curve is for clarity plotted with an offset of +1. **E.** Guinier plot for Svi3-3_d19 apo. **F.** Guinier plot for Svi3-3_d19 in presence of SAM.

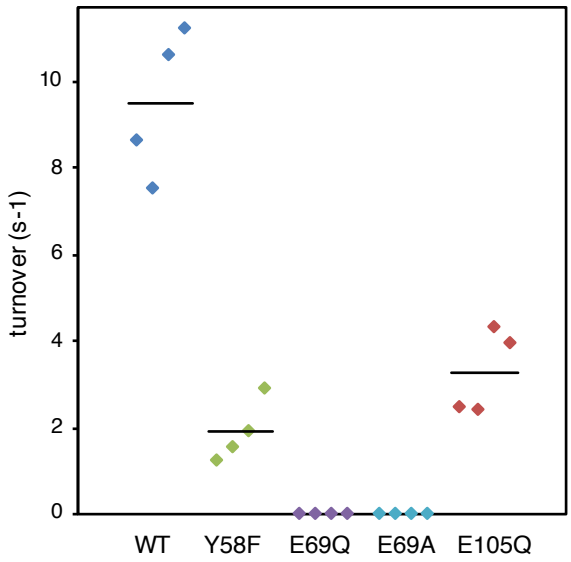

Figure S3. Enzymatic activity of Svi3-3 variants. Data is from technical duplicates from two different protein purifications (ordered from left to right) with the average represented by a black line. Calculated average activities +/- one standard deviation were: WT: 9.5 +/- 1.7 s^{-1}, Y58F: 1.9 +/- 0.7 s^{-1}, E69Q: 0.002 +/- 0.0006 s^{-1}, E69A: 0.007 +/- 0.0016 s^{-1}, E105Q: 3.3 +/- 0.99 s^{-1}

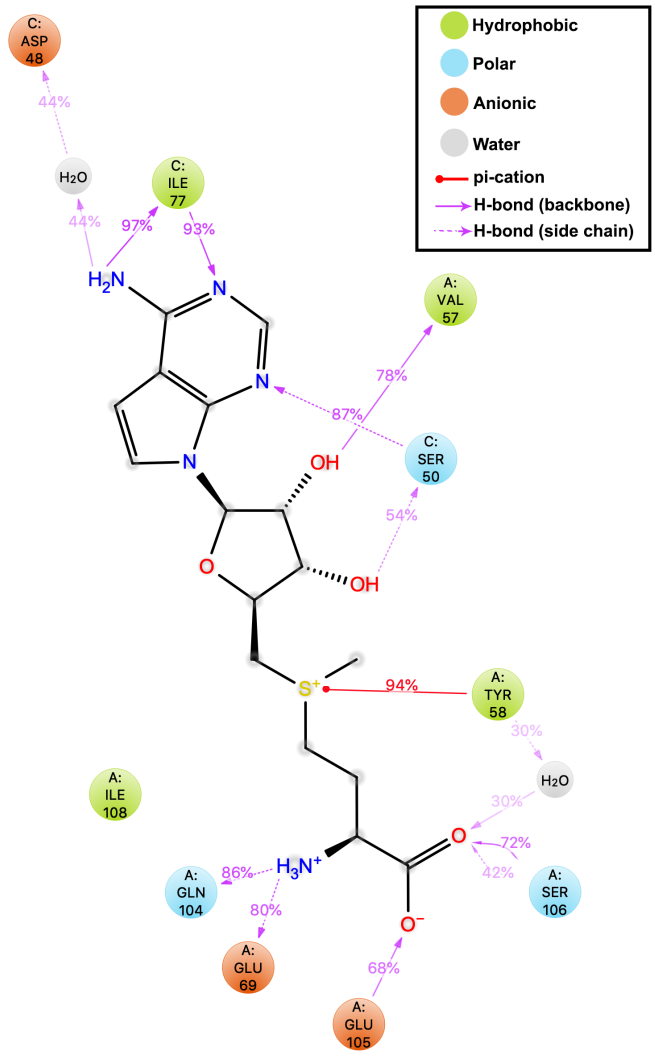

Figure S4. Protein-ligand interactions obtained from 100 ns MD simulations illustrating the percentage of interaction from the total simulation time.

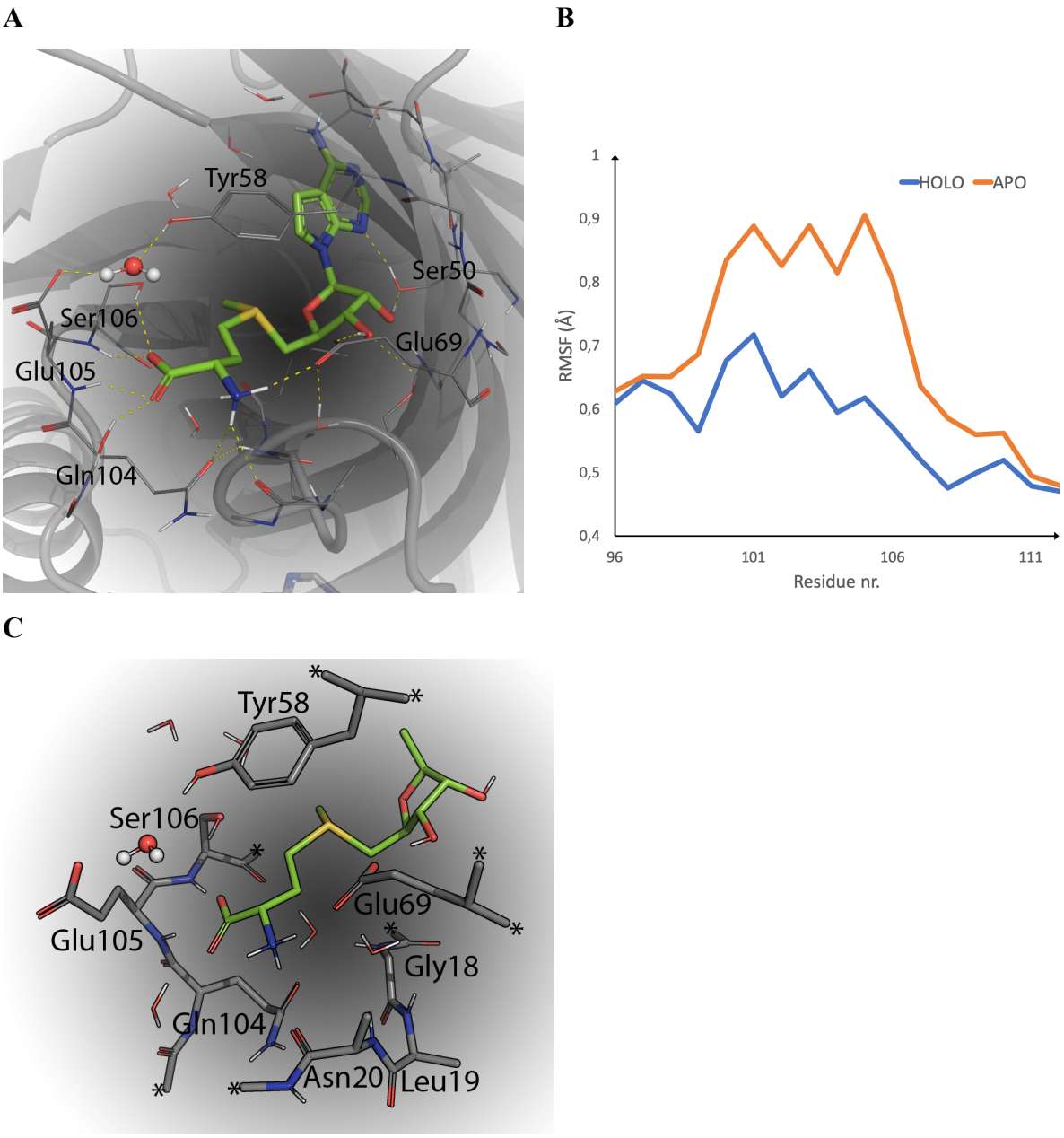

Figure S5. Computational modeling of Svi3-3 in complex with SAM. **A.** Snapshot from 100 ns MD simulations illustrating the dominant interactions for the methionine part of SAM in the active site. **B.** Average backbone root mean square fluctuation (RMSF) of active site residues 104 – 106 averaged over 100 ns MD simulation apo and holo. **C.** DFT cluster model utilized for the DFT calculations. Atoms marked with * are kept fixed during the calculations.

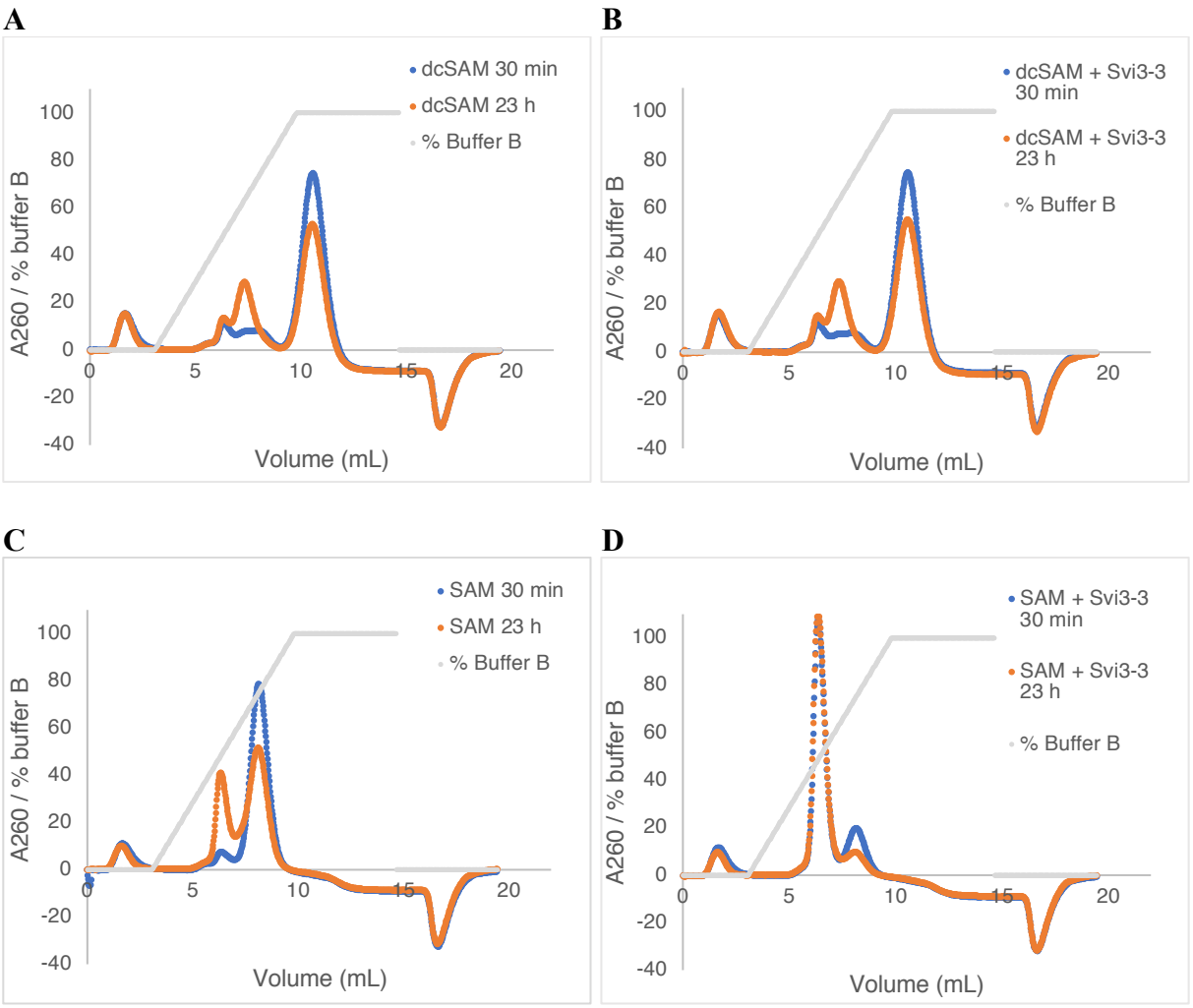

Figure S6. Ion exchange chromatography separation of dcSAM reactions and controls. **A.** 0.32 mM dcSAM mix (72 % dcSAM) incubated without enzyme **B.** 0.32 mM dcSAM mix (72 % dcSAM) incubated with 0.1 µM Svi3-3_d19 **C.** 0.32 mM SAM incubated without enzyme **D.** 0.32 mM SAM incubated with 0.1 µM Svi3-3_d19.

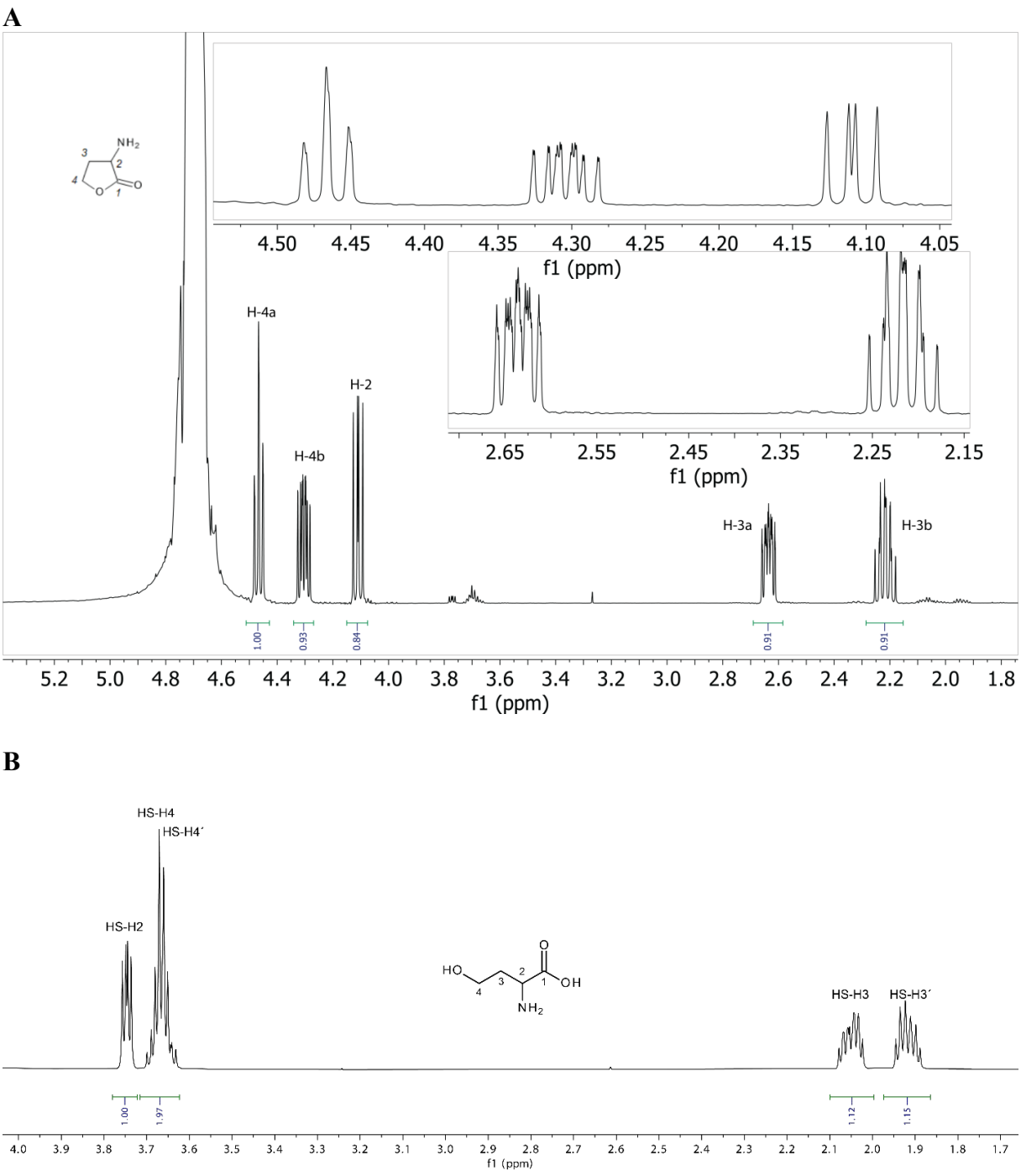

Figure S7. ^{1}H NMR spectra of reference samples. **A.** Homoserine lactone (600 MHz, 59 mM in sodium phosphate buffer, D_2O, pH 7.4). **B.** Homoserine (600 MHz, 57 mM in sodium phosphate buffer, D_2O, pH 7.4).

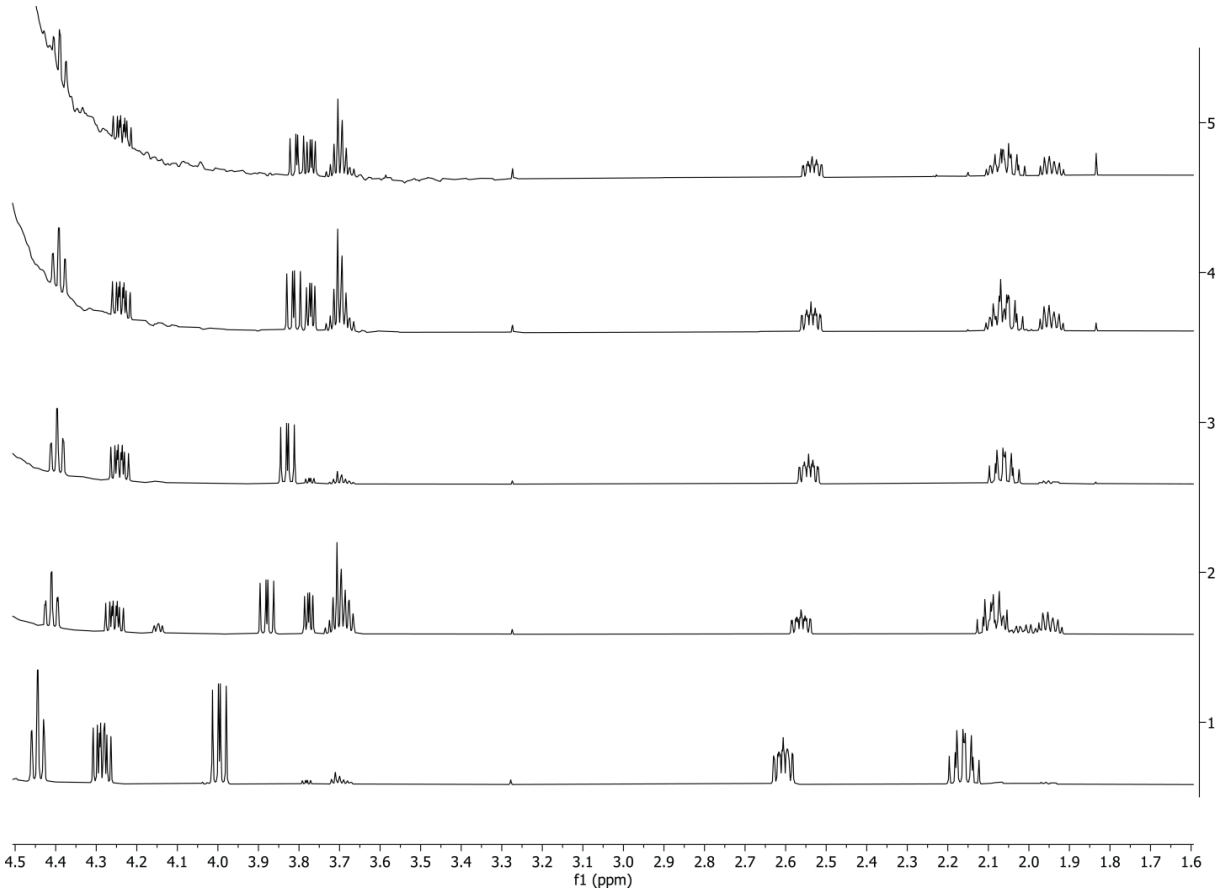

Figure S8. ^{1}H NMR spectra of a reference sample of homoserine lactone at various concentrations and exposure times to sodium phosphate buffer showing progressive hydrolysis to homoserine (600 MHz, sodium phosphate buffer, D2O, pH 7.4). Spectrum 1: 70 mM (t =0); spectrum 2: 17.5 mM (t = 50 min); spectrum 3: 4.4 mM (t =547 min); spectrum 4: 1.1 mM (t = 579 min); spectrum 5: 0.3 mM (t = 603 min).

Table S1: Sequences of Svi3-3 constructs in this study

Protein	Length (amino acids)	Sequence
Svi3-3_d19	165	MSGSHHHHHHGSSGENLYFQSLMERLGGGGFSARIFVGLNVGDKPTYTIE DVVKDTIAIKRQGILPDASFVAQRGVYTEQRSGQLVTENSVQIIIIDLEG LSKEDFTGKVQALGKELREDFKQESVIVEIQERGIVQDVYSITAEWYEEG PMRPLRVDLQPSLIS
Svi3-3_d19 after TEV cleavage	146	SLMERLGGGGFSARIFVGLNVGDKPTYTIEDVVKDTIAIRKRQGILPDAS FVAQRGVYTEQRSGQLVTENSVQIIIIDLEGLSKEDFTGKVQALGKELRE DFKQESVIVEIQERGIVQDVYSITAEWYEEGPMRPLRVDLQPSLIS

Table S2: *In vivo* complementation assay using different variants of Svi3-3, Orf1 and T3 SAMase, present on the IPTG-inducible plasmids pCA24N –gfp (Svi3-3 and Orf1) and pRD2 (T3 SAMase).

Strain numbers	Strain Genotype	M9 minimal media +IPTG (mM)	
		0	1
DA5438	wild-type	growth	growth
DA48933	*ΔilvA* + Svi3-3	no growth	growth
DA57022	*ΔilvA* + Svi3-3 E69Q	no growth	no growth
DA57021	*ΔilvA* + Svi3-3 E69A	no growth	no growth
DA51653	*ΔilvA* + Orf1	no growth	growth
DA67997	*ΔilvA* + Orf1 E50Q	no growth	no growth
DA67998	*ΔilvA* + Orf1 D51N	no growth	growth
DA57899	*ΔilvA*+ T3S	growth	no growth
DA58126	*ΔilvA*+ T3S E67Q	growth	no growth
DA58127	*ΔilvA* +T3S E68Q	no growth	no growth

Table S3: *In vivo* complementation assay using different variants of T3 SAMase, present on the chromosome

Strain	Strain Genotype	M9 minimal media + Arabinose (%)			
		0	0.01	0.05	0.1
DA5438	wild-type	growth	growth	growth	growth
DA58128	*ΔilvA*	no growth	no growth	no growth	no growth
DA67469	*ΔilvA*+ T3S	no growth	growth	growth	growth
DA67467	*ΔilvA*+ T3S E67Q	no growth	no growth	growth	growth
DA67468	*ΔilvA* +T3S E68Q	no growth	no growth	no growth	growth

Table S4: Primer sequences

Primer name	**Sequence**
Svi3-3_d19f	ATGGAACGTCTCGGCGGCGG
Svi3-3_r1	CTCAACTAATTAAGCTTGGCTGCAGG
Svi3-3_Y58F_f	GCTGCTCGGTGAAGACGCCGCGC
Svi3-3_Y58F_r	GCGCGGCGTCTTCACCGAGCAGC
Svi3-3_E69A_f	ACAGCTCGTCACGGCGAACTCGGTCCAGATCATC
Svi3-3_E69A_r	GATGATCTGGACCGAGTTCGCCGTGACGAGCTGT
Svi3-3_E105Q_f	CCACGATGACGCTCTGCTGCTTGAAATCCTC
Svi3-3_E105Q_r	GAGGATTTCAAGCAGCAGAGCGTCATCGTGG
araBAD_cat_sacB_F	AGTATAGCCTGGTTTCGTTTGATTGGCTGTGGTTTTATAC AGTCAGTGTAGGCTGGAGCTGCTTC
araBAD_cat_sacB_R	TCTCTACTGTTTCTCCATACCCGTTTTTTTGGATGGAGTGA AACGCATATGAATATCCTCCTTAGTTCC
T3SAM_int_catsacBF	CGTGCCGCACCGGGTCTTTATGGCTCCGTTGAGTCAACCG ATTTG GTGTAGGCTGGAGCTGCTTC
T3SAM_int_catsacBR	TTCCTCAGTTGGTGCGCTTGAGATTGCCTCACGATAGCAC CCGGTCATATGAATATCCTCCTTAGTTCC
ara_t3_SAMF	TCTCTACTGTTTCTCCATACCCGTTTTTTTGGATGGAGTGA AACGATGATTTTCACTAAAGAGCCTG
ara_t3_SAMR	AGTATAGCCTGGTTTCGTTTGATTGGCTGTGGTTTTATAC AGTCA TTATTGTACTTGCCAGCGGCGACC
Test_primer_f	ACCCCGCTTATTAAAAGCAT
Test_primer_r	AAATCCATCAAAAAACCAGG